

MASARYKOVA UNIVERZITA

Přírodovědecká fakulta

Ústav teoretické fyziky a astrofyziky

DIPLOMOVÁ PRÁCE

Kinetické modelování magnetosfér kompaktních objektů

Jakub Gazdoš

Vedoucí práce: Mgr. Jan Benáček, Ph.D.

Brno 2025



## Bibliografický záznam:

<b>Autor:</b>	Bc. Jakub Gazdoš Přírodovědecká fakulta, Masarykova univerzita Ústav teoretické fyziky a astrofyziky
<b>Název práce:</b>	Kinetické modelování magnetosfér kompaktních objektů
<b>Studijní program:</b>	N-FYZ Fyzika
<b>Studijní obor:</b>	Astrofyzika
<b>Vedoucí práce:</b>	Mgr. Jan Benáček, Ph.D.
<b>Akademický rok:</b>	2024/2025
<b>Počet stran:</b>	vi + 68
<b>Klíčová slova:</b>	kompaktní objekty, obecná teorie relativity, simulace, particle-in-cell simulace



## Bibliographic Entry:

**Author:** Bc. Jakub Gazdoš  
Faculty of Science, Masaryk University  
Department of physics and astrophysics

**Thesis Title:** Kinetic modeling of compact object magnetospheres

**Degree Programme:** N-FYZ Physics

**Field of Study:** Astrophysics

**Supervisor:** Mgr. Jan Benáček, Ph.D.

**Academic Year:** 2024/2025

**Number of Pages:** vi + 68

**Keywords:** compact objects, general relativity, simulations, particle-in-cell method



# Abstrakt

Cílem této práce je implementovat efekty zakřivení prostoročasu do particle-in-cell (PIC) simulačního kódu. Přístup pomocí “3+1” formalismu podle Komissarov (2004) značně zjednodušuje úsilí tím, že rozřezává čtyřrozměrný prostoročas na třírozměrné řezy absolutního prostoru, který je parametrizován univerzálním časem. To přináší dvě výhody: 1) rovnice mají známý tvar plochého časoprostoru, což umožňuje snadnější fyzikální interpretaci, a 2) univerzální časový parametr a časový krok v celé mřížce umožňují numerický přístup. Jiné PIC simulace úspěšně implementovaly efekty zakřivení a prokázaly jejich význam pro procesy v magnetosféře, jako je vytváření párů pro magnetosféry shodné s rotací hvězdy. Tato práce popisuje mou implementaci do PIC kódu ACRONYM, s předpokladem nerotujícího časoprostoru. Popisuji svou modifikaci časového vývoje elektromagnetického pole a testuji ji z hlediska numerické stability a fyzikální přesnosti. Představuji nové přístupy k výpočtu pohybu částic, interpolaci pole–částice a náboj zachovávajícímu výpočtu proudu v zakřiveném prostoročase. Upravený kód PIC byl otestován na změnách v disprezních relacích plazmatu v různých prostoročasech.

# Abstract

The aim of this work is to implement the effects of spacetime curvature into a particle-in-cell (PIC) simulation code. The “3+1” formalism approach developed by Komissarov (2004) greatly simplifies the effort by slicing the 4-dimensional spacetime into 3-dimensional slices of an absolute space, which is parametrised by a universal time. This brings two advantages: 1) the equations take on a familiar flat-spacetime form, allowing easier physical interpretation, and 2) the universal time parameter and timestep across the whole grid make it possible to approach numerically. Other PIC codes have successfully implemented the curvature effects and demonstrated their importance for the processes in the magnetosphere, such as pair creation for aligned magnetospheres. This work introduces my implementation into the PIC code ACRONYM, with the assumption of a non-rotating spacetime. I describe my modification of the electromagnetic field advancement and test it for numerical stability and physical accuracy. I also present novel approaches for computation of the particle pusher, field–particle interpolation, and charge-conserving current deposition in curved spacetime. The modified PIC code was tested on the changes in plasma dispersion relations depending on spacetime properties.



ZADÁNÍ  
DIPLOMOVÉ PRÁCE

Akademický rok: 2024/2025

---

**Ústav:** Ústav teoretické fyziky a astrofyziky

---

**Student:** Bc. Jakub Gazdoš

---

**Program:** Fyzika

---

**Specializace:** Astrofyzika

---

Ředitel ústavu PŘF MU Vám ve smyslu Studijního a zkušebního řádu MU určuje diplomovou práci s názvem:

---

**Název práce:** Kinetické modelování magnetosfér kompaktních objektů

---

**Název práce anglicky:** Kinetic modeling of compact object magnetospheres

---

**Jazyk práce:** angličtina

---

**Oficiální zadání:**

Magnetospheres of compact objects are physical laboratories of space, time, and matter in the most extreme conditions known in the Universe. The studies of compact objects strongly rely on investigations of their emitted radiation and gravitational wave properties. The observed radiation originates in their magnetospheres at scales that are necessary to be described by plasma kinetic models. However, the current kinetic plasma models still explain only some of the theoretically predicted properties of plasmas around compact objects.

The aim of the thesis is to include an approach at plasma kinetic scale into a particle-in-cell kinetic model of the compact object magnetosphere. The student will compare the selected process in the simulations of a compact object magnetosphere with the currently used approach.

**Plan of activities:**

- Study of the kinetic plasma models of compact object magnetospheres
- Design of the implementation into the current particle-in-cell kinetic model
- Implement and test the approach
- Carrying out simulations with realistic magnetosphere properties
- Process the data and investigate the differences in the evolution with the previously used case
- Compile the results into the thesis

**Literature:**

- Gurevich, A. V., Beskin, V. S., Istomin, Ya. N., & Cambridge University Press. Physics of the Pulsar Magnetosphere. (Cambridge University Press, 1993).
  - Philippov, A. & Kramer, M. Pulsar Magnetospheres and Their Radiation. 65 (2022).
  - ACRONYM Particle-in-cell kinetic code, Documentation page
-



# Poděkování

Děkuji vedoucímu práce Janu Benáčkovi za obětavou podporu, pomoc s návrhem implementace, nastavením simulace, interpretací výsledku a pečlivou kontrolu textu.

Děkuji Tatianě za předání zkušeností s kompilací kódu.

Děkuji Alence za důkladnou kontrolu textu.

Děkuji rodině za dlouhodobou podporu ve studiu.

# Prohlášení

Prohlašuji, že jsem svoji bakalářskou práci vypracoval samostatně pod vedením vedoucího práce s využitím informačních zdrojů, které jsou v práci citovány.

V Brně 5. května 2025

---

Jakub Gazdoš



# Contents

<b>Introduction</b>	<b>1</b>
<b>1 What is plasma?</b>	<b>2</b>
1.1 Plasma oscillations . . . . .	3
1.2 Langmuir electrostatic waves . . . . .	5
1.3 Electromagnetic waves . . . . .	5
<b>2 General relativity</b>	<b>7</b>
2.1 Electromagnetism . . . . .	9
2.2 Covariant derivative . . . . .	9
2.3 Christoffel symbols . . . . .	11
2.4 Curvature . . . . .	14
2.5 Spacetime around stars . . . . .	16
<b>3 Compact objects</b>	<b>18</b>
3.1 Compact object formation . . . . .	18
3.2 Black holes . . . . .	19
3.3 Neutron star magnetosphere . . . . .	19
3.4 Observational importance . . . . .	23
<b>4 Particle-in-cell (PIC) method</b>	<b>24</b>
4.1 Field evolution . . . . .	24
4.2 Particle motion . . . . .	26
4.3 Current deposition . . . . .	28
<b>5 Particle-in-cell equations in curved spacetime</b>	<b>31</b>
5.1 Declaration of spacetime . . . . .	31
5.2 Electromagnetic solver . . . . .	32
5.3 Particle pusher . . . . .	33
<b>6 Implementation in the ACRONYM PIC code</b>	<b>35</b>
6.1 Spacetime curvature . . . . .	35
6.2 1D Field solver . . . . .	36
6.3 2D Field solver . . . . .	40
6.4 Modified Boris push . . . . .	41
6.5 Field-particle interpolation . . . . .	44
6.6 Novel approach to current deposition . . . . .	45

<b>7 Plasma simulations</b>	<b>48</b>
7.1 1D Thermal plasma . . . . .	48
7.2 1D Plasma dispersion relations . . . . .	55
7.3 2D Thermal plasma . . . . .	58
7.4 2D Plasma dispersion relations . . . . .	63
<b>Conclusions</b>	<b>67</b>

# Introduction

Black holes and neutron stars remain one of the fascinating puzzles of astrophysics. To study their surroundings, we rely mostly on plasma simulations, which must take into account the influence of the massive objects on nearby spacetime predicted by general relativity. My thesis describes the work on the implementation of the curvature of spacetime in the equations used in particle-in-cell (PIC) kinetic plasma simulations, particularly the ACRONYM code. The first chapter introduces basic concepts of plasma physics, plasma oscillations, and electromagnetic waves in plasma. The second chapter describes the formalism and mathematical structures used in the theory of general relativity and the application on spacetime around compact objects. The third chapter talks about the formation of compact objects, models of neutron star magnetospheres, and the role of compact objects in astrophysical phenomena. The fourth chapter introduces basic concepts and equations of PIC simulations, which are then improved to include the effects of curvature in the fifth chapter. The detailed implementation into the ACRONYM code is described in the sixth chapter, along with the results of testing for numerical stability and accuracy. In the next chapter, I used the modified code to simulate a thermal plasma and study the change in plasma dispersion relations depending on the spacetime metric parameters. I simulate plasma in non-rotating systems, such as the Schwarzschild spacetime. The last chapter concludes the results and describes future improvements.

## Section 1:

### What is plasma?

This chapter was written with the help of the book Introduction to plasma physics by Chen (1984) and the notes on Plasma Astrophysics by Marian Karlický from the Astronomical Institute of the Czech Academy of Sciences.

Plasma is defined as a quasi-neutral gas of ionised particles showing collective behaviour. In a typical gas, the particles are electrically neutral and the motion of a particle is dictated by collisions with other particles. The influence of external forces acting upon the gas is mediated through these collisions. However, charged particles in a plasma can create local regions of non-zero charge, leading to electric fields, which in turn influence distant charged particles. The behaviour of a particle is then defined not only by the local properties but also by the overall state of the plasma. This leads to the concept of collisionless plasma, where long-range electromagnetic forces dominate over particle collisions to the point where collisions can be effectively ignored. A speciality of collisionless plasmas is that different particle species (electrons, protons, ions) can have, for example, different temperatures  $T_i$ , defined through the mean particle velocity of the species  $v_i^2 = k_B T_i / m_i$ , where  $k_B$  is the Boltzmann constant and  $m_i$  is the mass of the particle species.

To describe quasi-neutrality, we first have to introduce Debye shielding. Let us start with a neutral plasma with electron density  $n_e$ , electron temperature  $T_e$  and proton density  $n_p$ . We assume that the heavy protons are stationary relative to the electrons and create a homogeneous positive background charge. Then we put a positive charge  $q_0$  into the plasma that keeps a positive potential  $\phi_0$  at its location. This pulls nearby electrons into a negatively charged cloud around  $q_0$  with the same total charge as  $-q_0$ . If the electrons had no thermal motion, the cloud would remain intact, and the potential from the charge would be perfectly shielded from the rest of the plasma. However, electrons on the surface of the cloud only feel a weak potential and their kinetic energy is sufficient to escape the cloud. The shielding is then imperfect, and the potential spreads further into the plasma, leading to a non-zero electric field. The potential in the cloud is described by the Poisson equation

$$\nabla^2 \phi = -\frac{e(n_p - n_e)}{\epsilon_0},$$

where  $e$  is the elemental charge and  $\epsilon_0$  is the vacuum permittivity. Far from the charge, the electron density and the proton density are the same  $n_e = n_p$ . Inside the electron cloud, the electron gains potential energy  $e\phi$ . From the distribution

function

$$f(v_e) = A \exp \left\{ -\frac{\frac{1}{2}m_e v_e^2 - e\phi}{k_B T_e} \right\},$$

we obtain the electron density in relation to the potential

$$n_e = n_p \exp \left\{ \frac{e\phi}{k_B T_e} \right\}.$$

Due to the shielding, the potential falls off very quickly. That means for a majority of the cloud, we can approximate the electron density as a Taylor series

$$\nabla^2 \phi = -\frac{en_p}{\epsilon_0} \left[ 1 - \left( 1 + \frac{e\phi}{k_B T_e} \right) \right] = \frac{e^2 n_p}{\epsilon_0 k_B T_e} \phi.$$

This equation gives a solution

$$\phi = \phi_0 \exp \left\{ -\frac{r}{\lambda_D} \right\},$$

$$\lambda_D := \sqrt{\frac{\epsilon_0 k_B T_e}{e^2 n}},$$

where  $r$  is the distance from the centre of the cloud,  $\lambda_D$  is the characteristic size of the cloud also known as the Debye length. At distances greater than the Debye length, the potential is significantly weakened. In a hotter plasma the potential spreads out further, while a denser plasma is able to shield the potential more quickly.

Returning to quasi-neutrality, plasma is considered quasi-neutral when the characteristic length of the system  $L$  is much larger than the Debye length  $\lambda_D$ . That means that any local concentration of charge or external electric potential is shielded at a scale that leaves the majority of the plasma unaffected.

## 1.1 Plasma oscillations

The distribution of electrons in the plasma in the ion background is such that charge neutrality is achieved. When an electron is displaced from its equilibrium position, it creates an opposing electric field. Due to the imbalance of masses, the electron is pulled towards the heavier proton which stays approximately in place. Because of its momentum, the electron overshoots and oscillates around its equilibrium position.

Assuming no external magnetic field, no thermal motion, stationary ion background, infinite plasma, and displacement only in the x-direction, the oscillations

are purely electrostatic. We start with the equation of motion, continuity equation and Poisson equation

$$m n_e \left[ \frac{\partial \vec{v}_e}{\partial t} + (\vec{v}_e \nabla) \vec{v}_e \right] = -e n_e \vec{E}, \quad (1)$$

$$\frac{\partial n_e}{\partial t} + \nabla (n_e \vec{v}_e) = 0, \quad (2)$$

$$\nabla \vec{E} = \frac{\rho}{\epsilon_0} = \frac{e(n_i - n_e)}{\epsilon_0}. \quad (3)$$

Then we introduce perturbations of the physical quantities of the system

$$n_e = n_0 + \delta n, \quad \vec{v} = \vec{v}_0 + \delta \vec{v}, \quad \vec{E} = \vec{E}_0 + \delta \vec{E}.$$

In equilibrium, we assume homogenous electron distribution, stationary electrons and charge neutrality

$$\begin{aligned} \nabla n_0 = \vec{v}_0 = \vec{E}_0 = 0, \\ \frac{\partial n_0}{\partial t} = \frac{\partial \vec{v}_0}{\partial t} = \frac{\partial \vec{E}_0}{\partial t} = 0. \end{aligned}$$

Assuming that the perturbations are small, we can linearise the equations (1) and (2). Poisson equation (3) is simplified due to the fact that in equilibrium the densities are equal  $n_i = n_0$ :

$$m n_0 \frac{\partial \delta \vec{v}}{\partial t} = -n_0 e \delta \vec{E}, \quad (4)$$

$$\frac{\partial \delta n}{\partial t} + n_0 \nabla \delta \vec{v} = 0,$$

$$\nabla \delta \vec{E} = -\frac{e \delta n}{\epsilon_0}.$$

Assuming a sinusoidal profile of the oscillations in the x-direction (and  $\partial_t = -i\omega$ ,  $\nabla = ik$ )

$$-im\omega \delta v = -e \delta E,$$

$$-i\omega \delta n = -ik n_0 \delta v,$$

$$ik \delta E = -\frac{e \delta n}{\epsilon_0}.$$

Combining these three equations we get the frequency of the electron electrostatic oscillations, also known as the plasma frequency

$$\left( \omega^2 - \frac{n_0 e^2}{\epsilon_0 m} \right) \delta v = 0,$$

$$\omega_p = \sqrt{\frac{n_0 e^2}{\epsilon_0 m}}. \quad (5)$$

Based on the assumption we made earlier that the plasma is infinite, the electric fields induced by the oscillations cancel out and the total electric field is zero. In a case where the system is finite, the electric field at the surface of the system is non-zero and the plasma oscillations spread into other regions.

## 1.2 Langmuir electrostatic waves

Thermal motion of electrons can also cause propagation of plasma oscillations. This effect can be described by adding a pressure term to the equation of motion 1. Because we assume the plasma oscillations are planar, we can use the one-dimensional case

$$\frac{\partial p_e}{\partial x} = 3k_B T_e \frac{\partial n_e}{\partial x} = 3k_B T_e \frac{\partial \delta n}{\partial x},$$

Putting into the linearized equation of motion (4), we get

$$mn_0 \frac{\partial \delta \vec{v}}{\partial t} = -n_0 e \delta \vec{E} - 3k_B T_e \frac{\partial \delta n}{\partial x}.$$

Again, assuming a sinusoidal profile of the oscillations in the x-direction ( $\partial_t = -i\omega$ ,  $\nabla = ik_x$ ):

$$-imn_0 \omega \delta v = -en_0 \delta E - 3ikk_B T_e \delta n.$$

Using  $-i\omega \delta n = -ikn_0 \delta v$  and  $ik\delta E = -\frac{e\delta n}{\epsilon_0}$  from earlier, we get dispersion equations

$$-imn_0 \omega \delta v = en_0 \frac{e}{ik\epsilon_0} \frac{kn_0}{\omega} \delta v - 3ikk_B T_e \frac{kn_0}{\omega} \delta v,$$

$$\omega^2 \delta v = \frac{n_0 e^2}{\epsilon_0 m} \delta v + 3k^2 \frac{k_B T_e}{m} \delta v.$$

We recognise the plasma frequency and thermal velocity of electrons, obtaining the dispersion relation for the electrostatic Langmuir waves.

$$\omega^2 = \omega_p^2 + 3k^2 v_e^2. \quad (6)$$

## 1.3 Electromagnetic waves

We start with a plasma in an equilibrium state and introduce an electromagnetic wave, described as a perturbation to the electromagnetic field  $\delta \vec{E}$ ,  $\delta \vec{B}$ , which induces

a perturbation of electron velocity  $\delta\vec{v}$ , corresponding to a current  $j = -n_0e\delta\vec{v}$ . Taking perturbed Maxwell's equations

$$\nabla \times \delta\vec{E} = -\frac{\partial\delta\vec{B}}{\partial t}, \quad (7)$$

$$c^2\nabla \times \delta\vec{B} = -\frac{n_0e\delta\vec{v}}{\epsilon_0} + \frac{\partial\delta\vec{E}}{\partial t}. \quad (8)$$

Applying the rotation operator on equation (7) and taking the time derivative of equation (8) we get

$$\nabla \times (\nabla \times \delta\vec{E}) = \nabla(\nabla\delta\vec{E}) - \nabla^2\delta\vec{E} = -\nabla \times \frac{\partial\delta\vec{B}}{\partial t},$$

$$c^2\nabla \times \frac{\partial\delta\vec{B}}{\partial t} = -\frac{n_0e}{\epsilon_0} \frac{\partial\delta\vec{v}}{\partial t} + \frac{\partial^2\delta\vec{E}}{\partial t^2}.$$

Then assuming the perturbation in the form  $\exp\{i(\vec{k}\vec{r}-\omega t)\}$  and using equation (4), we combine the two equations into

$$-\vec{k}(\vec{k}\delta\vec{E}) + k^2\delta\vec{E} = -\frac{n_0e^2}{\epsilon_0mc^2}\delta\vec{E} + \frac{\omega^2}{c^2}\delta\vec{E}.$$

Electromagnetic waves are transverse  $\vec{k}\delta\vec{E} = 0$ , and we see the formula for plasma frequency  $\omega_p = \sqrt{n_0e^2/\epsilon_0m}$ , giving us the dispersion relation for electromagnetic waves in plasma.

$$\begin{aligned} (\omega^2 - \omega_p^2 - c^2k^2) \delta\vec{E} &= 0, \\ \omega^2 &= \omega_p^2 + c^2k^2. \end{aligned} \quad (9)$$

The formulas are derived for a plasma without an external magnetic field. Introducing an external magnetic field affects the motion of plasma particles, as well as the propagation of electromagnetic waves. This introduces additional modes and changes the dispersion relations.

## Section 2:

# General relativity

This chapter is written with the help of the books *Lecture Notes on General Relativity* by S. M. Carroll (1997) and *A First Course in General Relativity* by Schutz (2022).

In 1905, Albert Einstein published his theory of special relativity that introduced many revolutionary ideas such as length contraction and time dilation. Few years later, Minkowski proposed the idea of treating the time and spatial coordinates as four coordinates in a four-dimensional space. This led to the development of the theory of general relativity.

General relativity has two main postulates:

- 1) Principle of relativity: states that all laws of physics in all inertial frames are the same. This leads to the inability of an observer to measure whether he is in a moving or a stationary unaccelerated frame of reference.
- 2) Absolute speed of light: states that every unaccelerated observer measures the same value for the speed of light, regardless of the relative velocity of the observer and the light source.

Let's introduce an inertial frame described by four coordinates, where the coordinate  $t$  can be thought of as the global time that is universal for all points in a space that is mapped by the coordinates  $x, y, z$ . A "point" in this frame is called an event and is described by these four coordinates  $(t, x, y, z)$ . The distance between two events is then measured by the spacetime interval. For a simple flat universe also known as the Minkowski spacetime, the interval reads

$$ds^2 = -(cdt)^2 + dx^2 + dy^2 + dz^2.$$

For convenience, we shall adopt the natural unit system, in which the speed of light  $c = 1$ . We express the four coordinates as  $(t, x, y, z) = (x^0, x^1, x^2, x^3) = x^\mu$ . The Greek indices, such as  $\mu, \nu, \rho$ , range from 0 to 3, while Latin indices  $i, j, k$  range from 1 to 3 and refer to spatial components of tensors. Using this, the expression for the spacetime interval can be generalized

$$ds^2 = \sum_{\mu, \nu=0}^3 g_{\mu\nu} dx^\mu dx^\nu = g_{\mu\nu} dx^\mu dx^\nu,$$

where  $g_{\mu\nu}$  is the metric, and we use the summation convention, where indices appearing in both the superscript and subscript are summed over. Comparing with the previous expression, it is obvious that for the Minkowski spacetime it is almost

an identity matrix

$$\eta_{\mu\nu} = \begin{pmatrix} -1 & 0 & 0 & 0 \\ 0 & 1 & 0 & 0 \\ 0 & 0 & 1 & 0 \\ 0 & 0 & 0 & 1 \end{pmatrix}.$$

The Minkowski metric is vastly used and thus often denoted as  $\eta_{\mu\nu}$ . In general, the metric  $g_{\mu\nu}$  is a symmetric 4x4 tensor, can be used to lower indices of a vector  $g_{\mu\nu}x^\nu = x_\mu$ , and has an inverse that raises indices that satisfies

$$g_{\mu\rho}g^{\rho\nu} = \delta_\mu^\nu = \begin{cases} 1 & \mu = \nu, \\ 0 & \mu \neq \nu. \end{cases}$$

The spacetime interval is invariant under the Lorentz group. This group consists of rotations  $R_\mu^\nu$ , transformations involving two of the spatial coordinates, and boosts  $S_\mu^\nu$ , transformations involving a time coordinate and a spatial coordinate. For example, rotation in x-y plane with  $0 < \theta < 2\pi$  and boost in t-x plane with  $-\infty < \phi < \infty$  can be expressed as

$$R_\mu^\nu = \begin{pmatrix} 1 & 0 & 0 & 0 \\ 0 & \cos\theta & \sin\theta & 0 \\ 0 & -\sin\theta & \cos\theta & 0 \\ 0 & 0 & 0 & 1 \end{pmatrix}, \quad S_\mu^\nu = \begin{pmatrix} \cosh\phi & -\sinh\phi & 0 & 0 \\ -\sinh\phi & \cosh\phi & 0 & 0 \\ 0 & 0 & 1 & 0 \\ 0 & 0 & 0 & 1 \end{pmatrix}.$$

There is also the Levi-Civita symbol defined as

$$\epsilon_{\mu\nu\rho\sigma} = \begin{cases} 1 & \text{even permutation of indices,} \\ -1 & \text{odd permutation of indices,} \\ 0 & \text{otherwise (two or more indices repeat).} \end{cases}$$

We would like  $\epsilon_{\mu\nu\rho\sigma}$  to stay the same after raising indices. However, from linear algebra it follows that

$$\epsilon_{\mu\nu\rho\sigma}g^{\mu\alpha}g^{\nu\beta}g^{\rho\gamma}g^{\sigma\delta} = \det(g^{\mu\nu})\epsilon^{\alpha\beta\gamma\delta} = (g)^{-1}\epsilon^{\alpha\beta\gamma\delta},$$

where  $g = |\det(g_{\mu\nu})|$ . To resolve this, we define the Levi-Civita tensor as follows

$$e_{\mu\nu\rho\sigma} = \sqrt{|g|}\epsilon_{\mu\nu\rho\sigma},$$

$$e^{\mu\nu\rho\sigma} = \frac{\text{sgn}(g)}{\sqrt{|g|}}\epsilon^{\mu\nu\rho\sigma}.$$

It is then invariant to the lowering or raising of indices

$$e_{\mu\nu\rho\sigma}g^{\mu\alpha}g^{\nu\beta}g^{\rho\gamma}g^{\sigma\delta} = \sqrt{|g|}\epsilon_{\mu\nu\rho\sigma}g^{\mu\alpha}g^{\nu\beta}g^{\rho\gamma}g^{\sigma\delta} = \frac{\sqrt{|g|}}{g}\epsilon^{\alpha\beta\gamma\delta} = \frac{\text{sgn}(g)}{\sqrt{|g|}}\epsilon^{\alpha\beta\gamma\delta} = e^{\alpha\beta\gamma\delta}.$$

## 2.1 Electromagnetism

This chapter is written under the assumption of a flat Minkowski spacetime. The components of a covector and its contravector are equal; the position of the indices (raised, lowered) of the vectors  $E_\mu$  and  $B_\mu$  can be omitted.

The vectors describing the electric field  $E_i$  and the magnetic field  $B_i$  are invariant to the ordinary spatial rotations but not to the timespace boosts. We can construct the electromagnetic field strength tensor

$$F^{\mu\nu} = \begin{pmatrix} 0 & E_1 & E_2 & E_3 \\ -E_1 & 0 & B_3 & -B_2 \\ -E_2 & -B_3 & 0 & B_1 \\ -E_3 & B_2 & -B_1 & 0 \end{pmatrix}.$$

This tensor is invariant to the full Lorentz group. This allows us to conveniently transform the electromagnetic field into different reference frames. This result can lead to the notion that the electric field and the magnetic field are physically connected to each other in reference frame transformations, and each one is only a projection of this unified electromagnetic field that depends on the observer.

We define a current 4-vector  $J^\mu = (\rho, J^i)$  and write the Maxwell equations in index notation

$$\begin{aligned} e^{ijk} \partial_j B_k - \partial_0 E^i &= 4\pi J^i, \\ \partial_i E^i &= 4\pi J^0, \\ e^{ijk} \partial_j E_k + \partial_0 B^i &= 0, \\ \partial_i B^i &= 0. \end{aligned}$$

Using the components of the electromagnetic tensor  $F^{0i} = E^i$ ,  $F^{ij} = \epsilon^{ijk} B_k$ , the equations can be combined into two equations

$$\begin{aligned} \partial_\mu F^{\nu\mu} &= 4\pi J^\nu, \\ \partial_{[\mu} F_{\nu\rho]} &= \partial_\mu F_{\nu\rho} + \partial_\nu F_{\rho\mu} + \partial_\rho F_{\mu\nu} = 0. \end{aligned}$$

Both the classical form with four equations and this unified form with two equations are invariant under the Lorentz group. One advantage of the compact form is that it will be helpful in curved spacetime.

## 2.2 Covariant derivative

Let us look at how vector manipulation becomes complicated in curved space. When working in the Cartesian coordinate frame, we have a coordinate basis  $(\vec{e}_x, \vec{e}_y)$ . These basis vectors have constant length and point in the same direction

across the whole space,  $\partial_i \vec{e}_j = 0$ . Differentiating a vector in this frame is easy. Given a vector denoted as  $\vec{V} = V_x \vec{e}_x + V_y \vec{e}_y$ , then only the components of the vector are affected by the derivative, while the basis vector leave unchanged

$$\partial_x \vec{V} = \partial_x (V_x \vec{e}_x + V_y \vec{e}_y) = \partial_x (V_x) \vec{e}_x + \partial_x (V_y) \vec{e}_y.$$

This also shows that placing a vector at different points of the coordinate system does not change its components. For simplicity let's assume that the vector is parallel to the x-axis  $\vec{V} = V_x \vec{e}_x$  and the basis vector  $\vec{e}_x$  is a unit vector, then its length at two points  $x$  and  $x + \Delta x$  remains the same

$$\begin{aligned} |\vec{V}(x)| &= V_x |\vec{e}_x(x)| = V_x \\ |\vec{V}(x + \Delta x)| &= V_x |\vec{e}_x(x + \Delta x)| = V_x, \end{aligned}$$

where  $|\vec{V}|$  denotes vector length, and  $|x|$  denotes the absolute value. Hypothetically, if the basis vector length was a function of  $x$ , for example, the further from the origin the longer it gets  $|\vec{e}_x(x)| = |x|$ , then for the vector length to remain the same at different points of the grid  $x$  and  $x + \Delta x$

$$\begin{aligned} |\vec{V}(x)| &= |\vec{V}(x + \Delta x)| \\ V_x(x) |\vec{e}_x(x)| &= V_x(x + \Delta x) |\vec{e}_x(x + \Delta x)| \\ V_x(x) |x| &= V_x(x + \Delta x) |x + \Delta x| \\ \Rightarrow \frac{V_x(x + \Delta x)}{V_x(x)} &= \frac{|x|}{|x + \Delta x|}, \end{aligned}$$

the x-component of the vector would have to be the inverse function and get smaller as the vector is placed further from the origin.

In polar coordinates, the situation gets even more complicated. From the transformation between Cartesian and polar coordinates

$$\begin{aligned} x &= r \cos(\theta), \\ y &= r \sin(\theta), \end{aligned}$$

we can extract the transformation of the basis

$$\begin{aligned} \vec{e}_r &= \frac{\partial x}{\partial r} \vec{e}_x + \frac{\partial y}{\partial r} \vec{e}_y = \cos(\theta) \vec{e}_x + \sin(\theta) \vec{e}_y, \\ \vec{e}_\theta &= \frac{\partial x}{\partial \theta} \vec{e}_x + \frac{\partial y}{\partial \theta} \vec{e}_y = -r \sin(\theta) \vec{e}_x + r \cos(\theta) \vec{e}_y, \end{aligned}$$

$$\begin{aligned} |\vec{e}_r|^2 &= \cos^2(\theta) |\vec{e}_x|^2 + \sin^2(\theta) |\vec{e}_y|^2 = 1, \\ |\vec{e}_\theta|^2 &= r^2 \sin^2(\theta) |\vec{e}_x|^2 + r^2 \cos^2(\theta) |\vec{e}_y|^2 = r^2. \end{aligned}$$

From these formulas it is obvious that the basis vectors change their lengths depending on their position. However, they also change the direction they point in. We can uncover that by differentiation with respect to the coordinates

$$\begin{aligned}\frac{\partial \vec{e}_r}{\partial r} &= \frac{\partial}{\partial r}(\cos(\theta)\vec{e}_x + \sin(\theta)\vec{e}_y) = 0, \\ \frac{\partial \vec{e}_r}{\partial \theta} &= \frac{\partial}{\partial \theta}(\cos(\theta)\vec{e}_x + \sin(\theta)\vec{e}_y) = -\sin(\theta)\vec{e}_x + \cos(\theta)\vec{e}_y = \frac{1}{r}\vec{e}_\theta, \\ \frac{\partial \vec{e}_\theta}{\partial r} &= \frac{\partial}{\partial r}(-r\sin(\theta)\vec{e}_x + r\cos(\theta)\vec{e}_y) = -\sin(\theta)\vec{e}_x + \cos(\theta)\vec{e}_y = \frac{1}{r}\vec{e}_\theta, \\ \frac{\partial \vec{e}_\theta}{\partial \theta} &= \frac{\partial}{\partial \theta}(-r\sin(\theta)\vec{e}_x + r\cos(\theta)\vec{e}_y) = -r\cos(\theta)\vec{e}_x - r\sin(\theta)\vec{e}_y = -r\vec{e}_r.\end{aligned}$$

While differentiating a vector  $(V_r, V_\theta)$  in polar coordinates, then the inclusion of the change of the basis vector must not be forgotten

$$\begin{aligned}\frac{\partial \vec{V}}{\partial r} &= \frac{\partial}{\partial r}(V_r\vec{e}_r + V_\theta\vec{e}_\theta) \\ &= \left(\frac{\partial}{\partial r}V_r\right)\vec{e}_r + V_r\frac{\partial}{\partial r}\vec{e}_r + \left(\frac{\partial}{\partial r}V_\theta\right)\vec{e}_r + V_\theta\frac{\partial}{\partial r}\vec{e}_r.\end{aligned}$$

### 2.3 Christoffel symbols

A vector in a general coordinate system, in which the basis vectors can change their length and direction in relation to the position, is differentiated accordingly

$$\frac{\partial \vec{V}}{\partial x^\mu} = \frac{\partial V^\nu}{\partial x^\mu}\vec{e}_\nu + V^\nu \frac{\partial \vec{e}_\nu}{\partial x^\mu},$$

where  $\vec{e}_\mu$  are the basis vectors of a coordinate system with coordinates  $x^\mu$ . The change of the basis vectors is specific for a given coordinate system and can be expressed as a linear combination of the basis

$$\frac{\partial \vec{e}_\nu}{\partial x^\mu} = \Gamma_{\nu\mu}^\rho \vec{e}_\rho,$$

where  $\Gamma_{\alpha\beta}^\mu$  is called the Christoffel symbol. The index  $\nu$  denotes the basis vector being differentiated,  $\mu$  determines the coordinate with respect to which the differentiation is carried out and  $\rho$  tells us the component of the resulting vector. Using the Christoffel symbol, we can rewrite the derivative

$$\frac{\partial \vec{V}}{\partial x^\mu} = \frac{\partial V^\nu}{\partial x^\mu}\vec{e}_\nu + V^\nu \Gamma_{\nu\mu}^\rho \vec{e}_\rho.$$

The summing indices can be renamed, giving us a nice and simple expression

$$\frac{\partial \vec{V}}{\partial x^\mu} = \frac{\partial V^\nu}{\partial x^\mu} \vec{e}_\nu + V^\rho \Gamma_{\rho\mu}^\nu \vec{e}_\nu = \left( \frac{\partial V^\nu}{\partial x^\mu} + V^\rho \Gamma_{\rho\mu}^\nu \right) \vec{e}_\nu,$$

where the term in the parentheses is a tensor called the covariant derivative

$$\nabla_\mu V^\nu \equiv \frac{\partial V^\nu}{\partial x^\mu} + \Gamma_{\rho\mu}^\nu V^\rho.$$

We can construct a scalar  $\phi$  by multiplying a covariant vector  $V_\mu$  and a contravariant vector  $V^\mu$  and take its covariant derivative

$$\begin{aligned} \nabla_\nu \phi &= \nabla_\nu (V_\mu V^\mu) \\ &= (\nabla_\nu V_\mu) V^\mu + V_\mu \nabla_\nu V^\mu \\ &= \frac{\partial V_\mu}{\partial x^\nu} V^\mu + \tilde{\Gamma}_{\mu\nu}^\rho V_\rho V^\mu + V_\mu \frac{\partial V^\mu}{\partial x^\nu} + V_\mu \Gamma_{\rho\nu}^\mu V^\rho, \end{aligned}$$

where  $\tilde{\Gamma}_{\nu\mu}^\rho$  is some unknown Christoffel symbol for the covariant derivative of covariant vectors. Since a scalar does not depend on basis vectors, the covariant derivative must be equal to its ordinary partial derivative

$$\begin{aligned} \nabla_\nu \phi &= \nabla_\nu (V_\mu V^\mu) = \partial_\nu (V_\mu V^\mu) \\ &= \frac{\partial V_\mu}{\partial x^\nu} V^\mu + V_\mu \frac{\partial V^\mu}{\partial x^\nu}. \end{aligned}$$

Comparing the two results and renaming the summation indices gives us the relation

$$\tilde{\Gamma}_{\nu\mu}^\rho = -\Gamma_{\nu\mu}^\rho,$$

$$\nabla_\nu V_\mu \equiv \partial_\nu V_\mu - \Gamma_{\nu\mu}^\rho V_\rho.$$

The first derivative of the scalar depends on the basis vectors. The covariant derivative in Cartesian coordinates is equal to the partial derivative

$$\nabla_\mu \nabla_\nu \phi = \partial_\mu \partial_\nu \phi = \partial_\nu \partial_\mu \phi = \nabla_\nu \nabla_\mu \phi.$$

Since partial derivatives commute, the tensor of the second derivative is symmetric. If a tensor is symmetric in one basis  $T_{\mu\nu} = T_{\nu\mu}$ , performing a change of coordinates

$$T_{\mu\nu} = \frac{\partial x^\rho}{\partial x^\mu} \frac{\partial x^\sigma}{\partial x^\nu} T_{\rho\sigma} = \frac{\partial x^\rho}{\partial x^\mu} \frac{\partial x^\sigma}{\partial x^\nu} T_{\sigma\rho},$$

does not change its symmetry and it is symmetric in any basis. Using the definition of the covariant derivative in a general basis, we get that the Christoffel symbol is symmetric in any coordinate system

$$\begin{aligned}\nabla_\mu \nabla_\nu \phi &= \nabla_\nu \nabla_\mu \phi \\ \partial_\mu \partial_\nu \phi - \Gamma_{\nu\mu}^\rho \partial_\rho \phi &= \partial_\nu \partial_\mu \phi - \Gamma_{\mu\nu}^\rho \partial_\rho \phi \\ \Gamma_{\nu\mu}^\rho \partial_\rho \phi &= \Gamma_{\mu\nu}^\rho \partial_\rho \phi \\ \Gamma_{\nu\mu}^\rho &= \Gamma_{\mu\nu}^\rho.\end{aligned}$$

In Cartesian coordinates, the components of a covariant vector and its contravariant counterpart are equal

$$V_\mu = V^\mu,$$

and the covariant derivative is just the partial differentiation of the components. Then, the covariant derivatives of the two vector are the same

$$\nabla_\nu V_\mu = \frac{\partial}{\partial x^\nu} V_\mu = \frac{\partial}{\partial x^\nu} V^\mu = \nabla_\nu V^\mu.$$

In Cartesian coordinates the metric takes the form of Kronecker delta  $g_{\mu\nu} = \delta_{\mu\nu}$ . This means that, in Cartesian coordinates, the metric does not change the covariant derivative of the contravariant vector

$$\nabla_\nu V^\mu = g_{\mu\rho} \nabla_\nu V^\rho,$$

and the metric can be used to lower the indices of the contravariant derivative

$$\nabla_\nu V_\mu = \nabla_\nu V^\mu = g_{\mu\rho} \nabla_\nu V^\rho. \quad (10)$$

This is a tensor equation, which means it is true in all coordinate systems. Now, in a general coordinate system, the covector and contravector are connected by the metric

$$V_\mu = g_{\mu\rho} V^\rho.$$

Taking the covariant derivative of this equation gives us

$$\nabla_\nu V_\mu = \nabla_\nu (g_{\mu\rho}) V^\rho + g_{\mu\rho} \nabla_\nu V^\rho.$$

Comparing this with equation (10) we conclude that the metric is invariant to the covariant derivative

$$\nabla_\rho g_{\mu\nu} = \partial_\rho g_{\mu\nu} - \Gamma_{\rho\mu}^\sigma g_{\sigma\nu} - \Gamma_{\rho\nu}^\sigma g_{\mu\sigma} = 0,$$

which can be proven in a similar manner for the inverse metric. Expressing all three permutations of the covariant derivative of the metric gives us

$$\begin{aligned}\nabla_{\rho}g_{\mu\nu} &= \partial_{\rho}g_{\mu\nu} - \Gamma_{\rho\mu}^{\sigma}g_{\sigma\nu} - \Gamma_{\rho\nu}^{\sigma}g_{\mu\sigma} = 0, \\ \nabla_{\mu}g_{\nu\rho} &= \partial_{\mu}g_{\nu\rho} - \Gamma_{\mu\nu}^{\sigma}g_{\sigma\rho} - \Gamma_{\mu\rho}^{\sigma}g_{\nu\sigma} = 0, \\ \nabla_{\nu}g_{\rho\mu} &= \partial_{\nu}g_{\rho\mu} - \Gamma_{\nu\rho}^{\sigma}g_{\sigma\mu} - \Gamma_{\nu\mu}^{\sigma}g_{\rho\sigma} = 0.\end{aligned}$$

Subtracting the second and the third from the first and using the symmetry of the Christoffel symbol, we get

$$\partial_{\rho}g_{\mu\nu} - \partial_{\mu}g_{\nu\rho} - \partial_{\nu}g_{\rho\mu} + 2\Gamma_{\mu\nu}^{\sigma}g_{\sigma\rho} = 0,$$

which can be rearranged to obtain the formula for the components of the Christoffel symbols

$$\Gamma_{\mu\nu}^{\sigma} = \frac{1}{2}g^{\sigma\rho}(\partial_{\mu}g_{\nu\rho} + \partial_{\nu}g_{\rho\mu} - \partial_{\rho}g_{\mu\nu}).$$

## 2.4 Curvature

One may be curious to see, whether the covariant derivative commutes with itself  $[\nabla_{\nu}, \nabla_{\rho}]V^{\mu} = \nabla_{\nu}\nabla_{\rho}V^{\mu} - \nabla_{\rho}\nabla_{\nu}V^{\mu} = ?$ . Let's express the individual components first:

$$\begin{aligned}\nabla_{\nu}\nabla_{\rho}V^{\mu} &= \partial_{\nu}(\nabla_{\rho}V^{\mu}) - \Gamma_{\nu\rho}^{\sigma}\nabla_{\sigma}V^{\mu} + \Gamma_{\nu\sigma}^{\mu}\nabla_{\rho}V^{\sigma} \\ &= \partial_{\nu}(\partial_{\rho}V^{\mu} + \Gamma_{\rho\xi}^{\mu}V^{\xi}) - \Gamma_{\nu\rho}^{\sigma}(\partial_{\sigma}V^{\mu} + \Gamma_{\sigma\xi}^{\mu}V^{\xi}) + \Gamma_{\nu\sigma}^{\mu}(\partial_{\rho}V^{\sigma} + \Gamma_{\rho\xi}^{\sigma}V^{\xi}) \\ &= \partial_{\nu}\partial_{\rho}V^{\mu} + \partial_{\nu}\Gamma_{\rho\xi}^{\mu}V^{\xi} + \Gamma_{\rho\xi}^{\mu}\partial_{\nu}V^{\xi} \\ &\quad - \Gamma_{\nu\rho}^{\sigma}\partial_{\sigma}V^{\mu} - \Gamma_{\nu\rho}^{\sigma}\Gamma_{\sigma\xi}^{\mu}V^{\xi} + \Gamma_{\nu\sigma}^{\mu}\partial_{\rho}V^{\sigma} + \Gamma_{\nu\sigma}^{\mu}\Gamma_{\rho\xi}^{\sigma}V^{\xi},\end{aligned}$$

$$\begin{aligned}\nabla_{\rho}\nabla_{\nu}V^{\mu} &= \partial_{\rho}(\nabla_{\nu}V^{\mu}) - \Gamma_{\rho\nu}^{\sigma}\nabla_{\sigma}V^{\mu} + \Gamma_{\rho\sigma}^{\mu}\nabla_{\nu}V^{\sigma} \\ &= \partial_{\rho}(\partial_{\nu}V^{\mu} + \Gamma_{\nu\xi}^{\mu}V^{\xi}) - \Gamma_{\rho\nu}^{\sigma}(\partial_{\sigma}V^{\mu} + \Gamma_{\sigma\xi}^{\mu}V^{\xi}) + \Gamma_{\rho\sigma}^{\mu}(\partial_{\nu}V^{\sigma} + \Gamma_{\nu\xi}^{\sigma}V^{\xi}) \\ &= \partial_{\rho}\partial_{\nu}V^{\mu} + \partial_{\rho}\Gamma_{\nu\xi}^{\mu}V^{\xi} + \Gamma_{\nu\xi}^{\mu}\partial_{\rho}V^{\xi} \\ &\quad - \Gamma_{\rho\nu}^{\sigma}\partial_{\sigma}V^{\mu} - \Gamma_{\rho\nu}^{\sigma}\Gamma_{\sigma\xi}^{\mu}V^{\xi} + \Gamma_{\rho\sigma}^{\mu}\partial_{\nu}V^{\sigma} + \Gamma_{\rho\sigma}^{\mu}\Gamma_{\nu\xi}^{\sigma}V^{\xi}.\end{aligned}$$

Combining these two results and using commutativity of partial derivatives, symmetry of Christoffel symbols and renaming of summation indices, we get

$$[\nabla_{\nu}, \nabla_{\rho}]V^{\mu} = (\partial_{\nu}\Gamma_{\rho\xi}^{\mu} - \partial_{\rho}\Gamma_{\nu\xi}^{\mu} + \Gamma_{\nu\sigma}^{\mu}\Gamma_{\rho\xi}^{\sigma} - \Gamma_{\rho\sigma}^{\mu}\Gamma_{\nu\xi}^{\sigma})V^{\xi}.$$

The term in the parentheses is called the Riemann tensor

$$R_{\xi\nu\rho}^{\mu} = \partial_{\nu}\Gamma_{\rho\xi}^{\mu} - \partial_{\rho}\Gamma_{\nu\xi}^{\mu} + \Gamma_{\nu\sigma}^{\mu}\Gamma_{\rho\xi}^{\sigma} - \Gamma_{\rho\sigma}^{\mu}\Gamma_{\nu\xi}^{\sigma},$$

which describes the difference between the change of the vector moved first in the  $\mu$ -direction, second in the  $\nu$ -direction, and the change of the vector moved in the opposite order. Contracting the Riemann tensor gives us the Ricci tensor

$$R_{\xi\rho} := R_{\xi\mu\rho}^{\mu},$$

and contracting again by the inverse metric we get the Ricci scalar

$$R := g^{\mu\nu}R_{\mu\nu}.$$

The Ricci scalar is a simple indicator of the curvature of a metric. Let's explore that by, for example, looking at the metric of a sphere of radius  $r$

$$\begin{aligned} dl^2 &= r^2(d\theta^2 + \sin^2\theta d\phi^2), \\ g_{rr} &= r^2, \quad g_{\theta\theta} = r^2\sin^2\theta. \end{aligned}$$

Calculating the Christoffel symbols, Riemann and Ricci Tensors and finally the Ricci scalar

$$\begin{aligned} \Gamma_{\phi\phi}^{\theta} &= -\sin\theta\cos\theta, \\ \Gamma_{\phi\theta}^{\phi} &= \cotg\theta, \\ R_{\phi\theta\phi}^{\theta} &= \sin^2\theta, \\ R_{\theta\phi\theta\phi} &= g_{\theta\theta}R_{\phi\theta\phi}^{\theta} = r^2\sin^2\theta, \\ R_{\theta\theta} &= g^{\phi\phi}R_{\theta\phi\theta\phi} = 1, \\ R_{\phi\phi} &= g^{\theta\theta}R_{\theta\phi\theta\phi} = \sin^2\theta, \\ R &= g^{\theta\theta}R_{\theta\theta} + g^{\phi\phi}R_{\phi\phi} = 2r^{-2}. \end{aligned}$$

From this result, we can quickly see that the sphere has some curvature. It is always positive and decreases with increasing radius. Spaces that have a positive Ricci scalar are called positively curved, are similar to spherical surfaces and the surface in two perpendicular directions curves the same way. In the opposite case where the Ricci scalar is negative, the space is called negatively curved, the surface in two perpendicular directions is curved in the opposite way, like on a saddle. In general, the Ricci scalar can depend on a coordinate. In such a case the curvature changes depending on the location in the particular space. One such example is the surface of a torus.

## 2.5 Spacetime around stars

The energy-momentum tensor is defined as  $T_{\mu\nu}$ , where  $T_{00}$  is the energy density,  $T_{0i}$  are components of the momentum density and  $T_{ij}$  are components of the force density. The connection between matter and the curvature of spacetime is described by the Einstein field equation

$$G_{\mu\nu} = 8\pi GT_{\mu\nu},$$

where the Einstein tensor  $G_{\mu\nu} = R_{\mu\nu} - \frac{1}{2}g_{\mu\nu}R$  is connected to the metric, and  $G$  is the Newtonian gravitational constant. By choosing a distribution of matter, constructing the energy-momentum tensor and solving the Einstein field equations, one can obtain the metric of that particular system.

For the purpose of describing the spacetime around stars, one notable solution is the Schwarzschild metric, which is a vacuum solution  $T_{\mu\nu} = 0$ . It assumes a static spherically symmetrical system, ideal to describe a non-rotating star. In spherical coordinates  $(r, \theta, \phi)$  the spacetime interval can be denoted as

$$ds^2 = - \left(1 - \frac{R_S}{r}\right) dt^2 + \left(1 - \frac{R_S}{r}\right)^{-1} dr^2 + r^2 \sin^2 \theta d\phi^2 + r^2 d\theta^2,$$

where  $R_S = 2GM/c^2$  is called the Schwarzschild radius,  $M$  is the mass of the star, and  $c$  is the speed of light. The metric expressed in a matrix form is then

$$g_{\mu\nu} = \begin{pmatrix} 1 - \frac{R_S}{r} & 0 & 0 & 0 \\ 0 & \left(1 - \frac{R_S}{r}\right)^{-1} & 0 & 0 \\ 0 & 0 & r^2 \sin^2 \theta & 0 \\ 0 & 0 & 0 & r^2 \end{pmatrix}.$$

One may notice that the metric has two singularities: one at  $R = R_S$ , which is a mathematical singularity and can be removed by a transformation of the coordinate system, the other at  $R = 0$ , which is a physical singularity and is present in any coordinate system.

A more physically accurate model is a Kerr black hole, which introduces rotation to the description. It is an axially symmetric model with two parameters, the mass of the black hole  $M$  and the angular momentum with respect to the axis of

rotation  $J$ . The spacetime interval is calculated as

$$\begin{aligned}
 ds^2 = & -\frac{\Delta - a^2 \sin^2 \theta}{\rho^2} dt^2 - 2a \frac{2Mr \sin^2 \theta}{\rho^2} dt d\phi \\
 & + \frac{\rho^2}{\Delta} dr^2 + \frac{(a^2 + r^2)^2 - a^2 \Delta \sin^2 \theta}{\rho^2} \sin^2 \theta d\phi^2 + \rho^2 d\theta^2, \\
 \Delta := & r^2 - 2Mr + a^2, \quad \rho := r^2 + a^2 \cos^2 \theta, \quad a := \frac{J}{M}.
 \end{aligned}$$

For  $a \rightarrow 0$  it approaches the Schwarzschild black hole. The rotation of the black hole causes a dragging effect that can accelerate nearby particles and causes them to corotate. The ergosphere is a region where the corotation speed reaches the speed of light. The corotation also changes the shape of the event horizon, which is no longer described by the Schwarzschild radius.

---

## Section 3:

# Compact objects

This section is written with information mainly from the books *An introduction to modern astrophysics* by B. W. Carroll and Ostlie (2017) and *High Energy Astrophysics* by Longair (2011).

### 3.1 Compact object formation

At the end of their lifecycle, massive stars fuse heavier and heavier elements in their cores, with each step in the series of the elements requiring a higher temperature to ignite and being less efficient in liberating energy. At a central temperature of around  $10^9$  K electron-positron pairs start to form, these quickly annihilate and produce neutrinos that easily escape the interior of the star and carry a large portion of the energy away. This phenomenon adds to the inefficiency of later stages in the fusion sequence, meaning that the time-scales get shorter and shorter. The last stage lasts only a few days and fuses silicon into iron nuclei  $^{56}\text{Fe}$ , reactions that produce heavier nuclei are endothermic and extract energy from the core.

As the iron core heats up, additional processes start that weaken the star's ability to resist its collapse. First, energetic electrons begin to interact with protons and form neutrons through the inverse  $\beta$ -decay, producing neutrinos, leading to more energy loss. Second, highly energetic  $\gamma$ -photons start to disintegrate heavy nuclei into lighter ones, removing thermal energy from the core and producing a large amount of free neutrons and protons that again combine with electrons and lead to high energy loss. With most of the produced energy being carried out of the core by neutrinos and the weakening of the electron degeneracy pressure, the core rapidly collapses. Because information from the core travels at the speed of sound and the collapse is very rapid, the core decouples into an collapsing inner core and an outer core, which is delayed in its collapse. The collapse is stopped when the material is so dense that the Pauli exclusion principle applies to neutrons. The inner core bounces outward and collides with the outer core that has also started to collapse in the mean time. This creates a shock wave in the core, increasing the density and temperature. The high temperature results in photodisintegration of heavy nuclei producing free protons that interact with free electrons to form neutrons and neutrinos. The density climbs so high that the highly energetic neutrinos are captured. This process releases an enormous amount of energy in a short burst of time, resulting in a supernova explosion that blows away the surrounding atmosphere, exposing the dense hot iron core.

The extreme conditions present in the core after the collapse crush the heavy

nuclei and electrons and transform them into an extremely dense material that resists further contraction by neutron degeneracy pressure, creating a neutron star. Due to the conservation of angular momentum, the sudden shrink in radius forces the neutron star to spin up to unbelievable frequency, shortening the period to about a millionth of the period of the former core, resulting in a rotational period of a few milliseconds.

### 3.2 Black holes

There is an upper limit on the mass of neutron stars, called the Tolman-Oppenheimer-Volkoff limit, ranging from  $2.2 M_{\odot}$  for a static case to  $2.9 M_{\odot}$  for rapidly rotating ones. The collapse of a core exceeding this mass limit cannot be stopped even by the neutron degeneracy pressure and the material is crushed into a black hole. The radius of a black hole is described by the event horizon. For a non-rotating black hole it is the Schwarzschild radius  $R_S = \frac{2GM}{c^2}$ , the radius at which the escape velocity of the gravitational well is equal to the speed of light. Crossing below the event horizon causes any matter as well as light to fall inward and prevents it from ever escaping. This means that no light can be emitted from the surface of a black hole and travel outward for us to detect. A rotating black hole introduces a dragging effect that forms a region called the ergosphere around the event horizon where infalling particles are forced to corotate at the speed of light, and the event horizon changes its shape. If one were to look toward a black hole, they would only observe a black disk, a shadow obscuring the background of stars. As direct observation of light from a black hole is impossible, only the gravitational influence on the surrounding matter can be studied. A black hole is thus characterized by three parameters that dictate the curvature of the surrounding spacetime, the mass  $M$ , the charge  $Q$  and its spin angular momentum  $J$ .

### 3.3 Neutron star magnetosphere

Another consequence of the core collapse is the amplification of the magnetic field. The magnetic field lines are frozen into the conducting matter, which means the magnetic flux,  $\Phi_0$ , going through the surface is conserved during the collapse

$$\Phi_0 = B_0 4\pi R_0^2 = \Phi_{NS} = B_{NS} 4\pi R_{NS}^2.$$

Since the radius rapidly falls, the magnetic field of the neutron star must increase greatly to conserve the magnetic flux. Typical neutron stars carry magnetic fields on the order of  $10^8$  T, much larger compared to the Sun's global magnetic field  $B_{\odot} = 2 \times 10^{-4}$  T.

The model of neutron star magnetospheres described in the following paragraphs is based on the review of Philippov and Kramer (2022). Magnetospheres of typical

neutron stars are approximated as dipolar, with the axis of the dipole generally not aligned with the rotational axis. The material inside the neutron star is assumed to be superconducting  $\sigma \rightarrow \infty$ . From equations of magnetohydrodynamics and assuming rigid rotation it arises that the electric field inside the star  $\vec{E} = -\vec{v} \times \vec{B}/c = (\vec{\Omega} \times \vec{r}) \times \vec{B}/c$ , where  $\vec{\Omega}$  is the star rotation vector and  $\vec{r}$  is the position vector. A model of the electric field satisfying this condition and the Poisson's equation implies strong electric fields at the surface parallel to the magnetic field  $\vec{E} \cdot \vec{B} \neq 0$ . The electric fields can pull charged particles from the star, filling the surroundings and creating a plasma magnetosphere. Polarisation currents of this plasma screen the electric field and lower the extraction of charged particles. A steady state of this system is achieved when the electric field in the frame of the moving plasma vanishes. In the outside frame, this corresponds to the frozen-in condition  $\vec{E} = \vec{v} \times \vec{B}$  and  $\vec{E} \cdot \vec{B} = 0$ .

When the steady state  $\vec{E} \cdot \vec{B} = 0$  is assumed to hold for the whole magnetosphere, we get the condition for the electric field  $\vec{E} = (\vec{\Omega} \times \vec{r}) \times \vec{B}/c$ , the magnetosphere corotates with the neutron star. As we move farther from the surface, the corotation speed approaches the speed of light, reaching it at the radius  $R_c$ , which marks the "light cylinder." Magnetic field lines that fit inside the light cylinder are closed and retain plasma. In contrast, magnetic field lines that touch the light cylinder are unwound and open up to infinity because the plasma corotation velocity cannot exceed the speed of light. These are called open magnetic field lines, and the region near the surface of the neutron star where they originate is labelled as the polar cap region. The plasma in open magnetic field lines escapes the magnetosphere, carrying energy away from the neutron star and slowing its rotation.

As the plasma in the polar cap region is not contained, the screening of the electric field does not occur and electrons are accelerated to high Lorentz factors. The energetic primary electrons travel along curved magnetic field lines and emit  $\gamma$ -ray photons as a result of curvature radiation. These photons then interact with the strong magnetic field and undergo single-photon conversion into an electron-positron pair,  $\gamma + B \rightarrow e^- + e^+$ . The new pair is again accelerated and emits  $\gamma$ -rays in a similar fashion, creating a cycle that produces a dense secondary plasma. This "pair cascade" eventually screens the electric field, weakening the acceleration and disallowing the creation of secondary particles. When the secondary plasma leaves the vicinity of the polar cap region, the process repeats, creating a series of plasma clumps. The region between the star surface and the point where the pair cascade takes place and in which primary electrons are accelerated is called the gap region.

The energetic particles produced in the polar cap region continue their journey along the magnetic field lines and emit a radio beam due to curvature radiation. As the neutron star rotates, this beam may get directed towards Earth. When this happens, astronomers observe periodic radio pulses with very short periods,

in the order of seconds or milliseconds, and extremely precise timing. They were first discovered by Jocelyn Bell in 1967, first published by Hewish et al. (1968) and soon named pulsars.

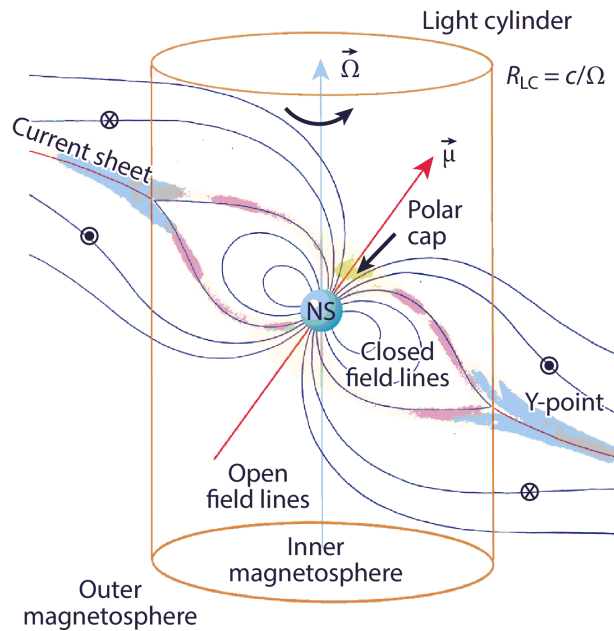


Figure 1: Model of a neutron star magnetosphere. Closed field lines trap plasma which corotates with the neutron star. At the light cylinder radius the corotation velocity exceeds the speed of light and the plasma escapes opening up the magnetic field lines. Credit: Philippov and Kramer (2022)

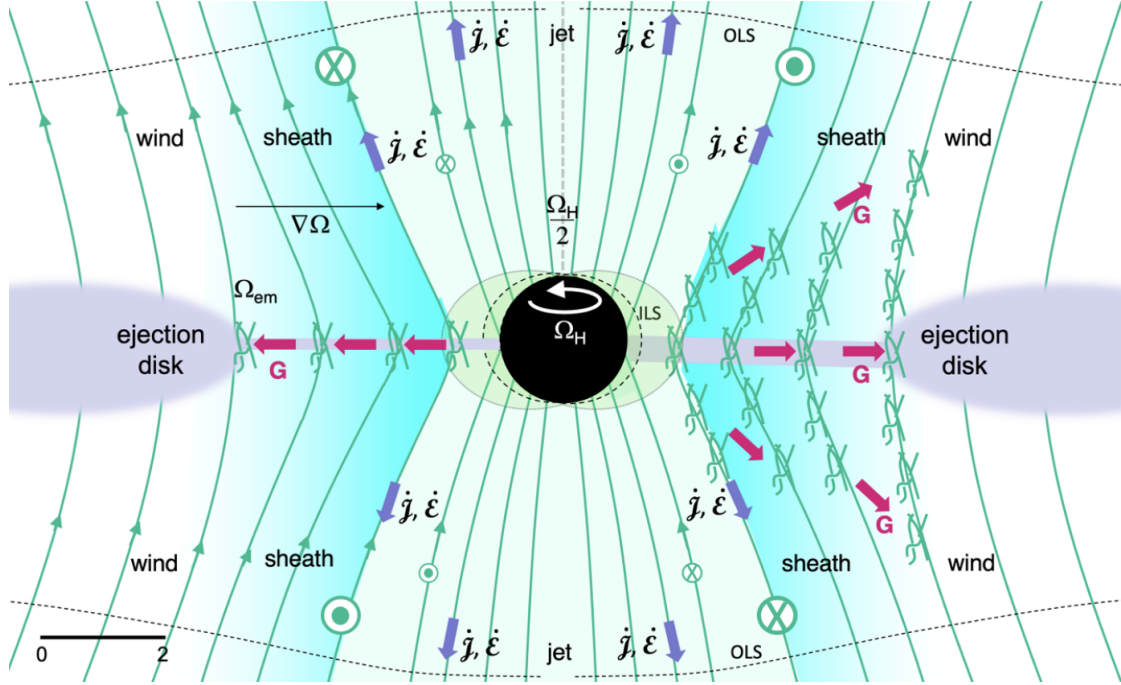


Figure 2: Model of a black hole magnetosphere. The black circle represents the Event Horizon that traps any matter or light that enters, the elliptical area around the event horizon is the ergosphere. The dotted lines describe the inner light surface (ILS), below which an observer at rest with the reference frame falls inward, and the outer light surface (OLS), above which the observer at rest moves outward. The light green lines represent the projection of the magnetic field lines onto the plane of the figure, which spins with the black hole at half the corotation speed  $\Omega_H/2$ . The spinning magnetic field develops instabilities within a thin ejection disk producing torque  $G$ . Therefore, rotational energy  $\dot{\mathcal{E}}$  and angular momentum  $\dot{\mathcal{J}}$  is extracted from the black hole and transported to the surrounding material, creating magnetocentrifugal wind. When the gas flows outward due to centrifugal force, its inertia decreases its angular rotation, depicted by the gradient  $\nabla\Omega$ , and the magnetic field lines, which are embedded into the gas, are dragged along and twisted. The direction of the twist is portrayed by the  $\otimes$ ,  $\odot$  symbols. The twisted magnetic field and the dynamical pressure of the disk drive the collimation of jets. The outer boundary of the jets is surrounded by a current sheath, depicted in light blue. Credit: Blandford and Globus (2022).

---

### 3.4 Observational importance

These compact objects play an important role in many astrophysical phenomena. The extremely short periodic pulsations of pulsars were already tied to the radio beam of a rapidly rotating neutron star. The high precision of the pulses is used in pulsar timing arrays to detect small deviations in their timing and can help to uncover cosmic gravitational waves. Pulsars are also a source of energy that accelerates surrounding material left from the supernova explosion. This pulsar wind creates pulsar wind nebulae that are observed across the electromagnetic spectrum.

Both neutron stars and black holes have been observed to host accretion disks and jets. Super-massive black holes (SMBHs), characterised by their mass in the order of  $10^6 - 10^9 M_{\odot}$ , are located in the centre of most galaxies. When there is ongoing accretion of matter onto the SMBH, we observe an active galactic nucleus (AGN) that outshines the whole stellar component of the galaxy and plays a crucial role in its evolution affecting the mixing of the intergalactic medium and stellar formation.

In recent years, the fascinating study of gravitational waves has been brought into public perception after their first direct measurement by the LIGO Collaboration in 2015. The type of gravitational waves measured in this discovery is created by a merger of two massive compact objects, in this case two stellar-mass black holes. From theory, a merger of a black hole and a neutron star or of two neutron stars also produces gravitational waves, although much fainter and harder to detect. These mergers are additionally connected to short-hard gamma-ray bursts, and kilonovae, one of the most luminous phenomena in the universe.

Our understanding of these compact objects and the interaction with the surrounding matter is thus crucial for further research in other astrophysical branches. To obtain the full picture of the nature of these compact objects we need to study the plasma in their vicinity and the associated processes, such as particle acceleration, emission processes, accretion and jet production.

## Section 4:

# Particle-in-cell (PIC) method

This chapter introduces the basics of particle-in-cell simulations: the configuration of particles and the electromagnetic field, the equations dictating the time evolution of the system and their corresponding numerical algorithms. The equations presented in this chapter take the value of speed of light  $c = 1$ .

In contrast to the magneto-hydrodynamic (MHD) simulations, which describe the plasma as a fluid, the idea of the particle-in-cell approach is to simulate the plasma self-consistently at kinetic scales in an electromagnetic field. This allows us to capture important physical processes at the microscopic scales that are not resolved by the MHD method. The need to simulate a large number of particles caused by the high plasma density required to observe the studied plasma properties and processes may paint this approach as unfeasible, even impossible.

The first way to significantly reduce the computational load is to replace the direct Coulomb interaction of the individual particles by the indirect interaction of the particles through the electromagnetic field. One moving charged particle represents arbitrary current that induces an electric field that affects another particle through the Lorentz force. This greatly reduces the scaling of the number of interactions and calculations from  $N^2$  to  $N$ .

The second approach is to implement a macroparticle that represents a large number of real physical particles, having the appropriate charge and mass, while counting as a single particle in the numerical procedure. The number of particles represented is called the macroparticle factor and can vary for each macroparticle.

### 4.1 Field evolution

The electromagnetic fields are evolved in each time step according to Maxwell's equations, particularly the Faraday and the Ampère–Maxwell law.

$$\partial_t \vec{B} = -\nabla \times \vec{E}, \quad (11)$$

$$\partial_t \vec{E} = \nabla \times \vec{B} - 4\pi \vec{J}. \quad (12)$$

The numerical scheme used in this thesis is based upon the the finite difference time domain (FDTD) method by Yee (1966). In this method, the components of the electromagnetic field are staggered both in space and time, as described by Figure (3). The staggered spatial configuration is known as the Yee lattice, the staggered time evolution is called the leapfrog scheme. For example, the time

evolution of  $B_z$  in this scheme is discretized as

$$\frac{B_z|_{i+1/2,j+1/2,k}^{n+1/2} - B_z|_{i+1/2,j+1/2,k}^{n-1/2}}{\Delta t} = - \frac{E_y|_{i+1,j+1/2,k}^n - E_y|_{i,j+1/2,k}^n}{\Delta x} + \frac{E_x|_{i+1/2,j+1,k}^n - E_x|_{i+1/2,j,k}^n}{\Delta y},$$

where subscripts  $i, j, k$  describe position in the Yee lattice, superscript  $n$  is the temporal index,  $\Delta t$  is the time step and  $\Delta x, \Delta y$  are lengths of a grid cell. Gauss's

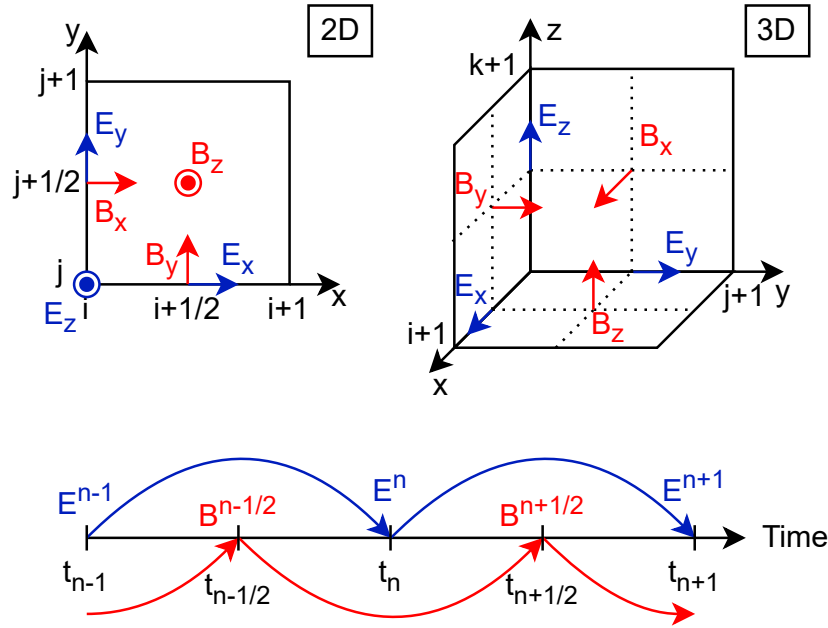


Figure 3: Top: the spatial staggering of the components of the electromagnetic field in the Yee lattice. Bottom: the temporal staggering of the electric and the magnetic field.

law  $\nabla \cdot \vec{E} = \rho$  is occasionally used to correct errors in the electric field that arise due to numerical inaccuracy inherent to the discretization of the derivatives. This numerical procedure conserves the divergence-free property of the magnetic field. If the initial magnetic field satisfies the condition  $\nabla \cdot \vec{B} = 0$ , it holds for the entire simulation.

## 4.2 Particle motion

The motion of particles is dictated by the Lorentz force, giving us a set of equations:

$$\frac{d\vec{x}}{dt} = \frac{\vec{u}}{\Gamma}, \quad (13)$$

$$\frac{d\vec{u}}{dt} = \frac{q}{m} \left( \vec{E} + \frac{\vec{u} \times \vec{B}}{\Gamma} \right), \quad (14)$$

where  $\vec{u} = \Gamma\vec{v}$ ,  $\Gamma = \sqrt{1 - v^2}$  and  $\vec{v}$  is the velocity of the particle in units of speed of light.

The common numerical scheme to solve these equations is the Boris push by Boris and Shanny (1971). Similarly to the Yee method for the field solver, the position vector  $\vec{x}$  and velocity vector  $\vec{u}$  are staggered in time, where the position is placed at whole time steps  $\vec{x}^n, \vec{x}^{n+1}$  and the velocity resides at half time steps  $\vec{u}^{n-1/2}, \vec{u}^{n+1/2}$ . The new particle position is calculated as

$$\vec{x}^{n+1} = \vec{x}^n + \frac{\vec{u}^{n+1/2}}{\Gamma} \Delta t.$$

To solve the equation (14) discretized as

$$\frac{\vec{u}^{n+1/2} - \vec{u}^{n-1/2}}{\Delta t} = \frac{q}{m} \left( \vec{E}^n + \frac{\vec{u}^n \times \vec{B}^n}{\Gamma^n} \right),$$

$\vec{u}^n$  is first replaced by  $(\vec{u}^{n+1/2} + \vec{u}^{n-1/2})/2$ . Then two helpful variables are introduced

$$\begin{aligned} \vec{u}^- &= \vec{u}^{n-1/2} + \frac{q\vec{E}^n}{2m} \Delta t, \\ \vec{u}^+ &= \vec{u}^{n+1/2} - \frac{q\vec{E}^n}{2m} \Delta t, \end{aligned}$$

that allow us to decompose it into three steps

$$\begin{aligned} \vec{u}^- &= \vec{u}^{n-1/2} + \frac{q\vec{E}^n}{2m} \Delta t, \\ \vec{u}^+ &= \vec{u}^- + \frac{q}{2m} \frac{(\vec{u}^+ + \vec{u}^-) \times \vec{B}^n}{\Gamma^n} \Delta t, \\ \vec{u}^{n+1/2} &= \vec{u}^+ + \frac{q\vec{E}^n}{2m} \Delta t. \end{aligned}$$

The first is a half step acceleration by the electric field, second is the rotation of the velocity vector by the magnetic component, and last is the second half acceleration

by the electric field. The second step however includes  $\vec{u}^+$  on the right side in the cross product. This can be solved by introducing

$$\begin{aligned}\vec{f}_1 &= \frac{q\Delta t}{2m\Gamma^n} \vec{B}^n, \\ \vec{u}' &= \vec{u}^- + \vec{u}^- \times \vec{f}_1, \\ \vec{f}_2 &= \frac{2\vec{f}_1}{1 + (\vec{f}_1)^2}, \\ \vec{u}^+ &= \vec{u}^- + \vec{u}' \times \vec{f}_2,\end{aligned}$$

where  $\Gamma^n = \sqrt{1 + (\vec{u}^-)^2}$ .

One may take notice that this scheme requires the magnetic field at a whole timestep  $\vec{B}^n$ , while the leapfrog scheme assumes the magnetic field is known at half timesteps  $n - 1/2, n + 1/2$ . In practice, the simulation starts with an initial electric and magnetic field at time  $t_0$ . The first step is a half step of the magnetic field  $\vec{B}^{t_0}$  using  $\vec{E}^{t_0}$  to time  $t_0 + 1/2$ , getting  $\vec{B}^{t_0+1/2}$ . Then we follow with a whole step of the electric field  $\vec{E}^{t_0}$  to  $\vec{E}^{t_0+1}$  using the half step value  $\vec{B}^{t_0+1/2}$  and complete the cycle by taking a half step from  $\vec{B}^{t_0+1/2}$  to  $\vec{B}^{t_0+1}$  by using  $\vec{E}^{t_0+1}$ . The method is depicted in the Figure (4). While it increases the number of calculations, the concept of taking half step jumps with the magnetic field preserves the second order accuracy of the leapfrog scheme while eliminating the time staggering of the electric and magnetic field that in turn simplifies the numerical calculations of the particle motion. Another solution could be to take a time average of the half-timestep magnetic fields to obtain the required whole-timestep value.

Because the particle is located at an arbitrary position  $(x, y, z)$  of the grid cell while the electric and magnetic fields are located at fixed points  $(x_i, y_i, z_i)$ , there has to be an interpolation of the fields to the position of the particle. That is done by the so-called form factors or form functions  $S(|x_i - x|)$ , that assign a weight to the values of the fields in nearby cells depending on their distance from the particle  $|x_i - x|$ , with the condition that the weights sum to one

$$\vec{E}(x, y, z) = \sum_{ijk} \vec{E}_i S(|x_i - x|) S(|y_j - y|) S(|z_k - z|). \quad (15)$$

The number of nearby cells used and the distance dependency is given by the chosen form factor. For example, the cloud-in-cell (CIC) scheme is a linear first order interpolation that uses two neighbouring cells

$$S(|x_i - x|) = \begin{cases} 1 - \frac{|x_i - x|}{\Delta x} & |x_i - x| < \Delta x, \\ 0 & |x_i - x| > \Delta x. \end{cases}$$

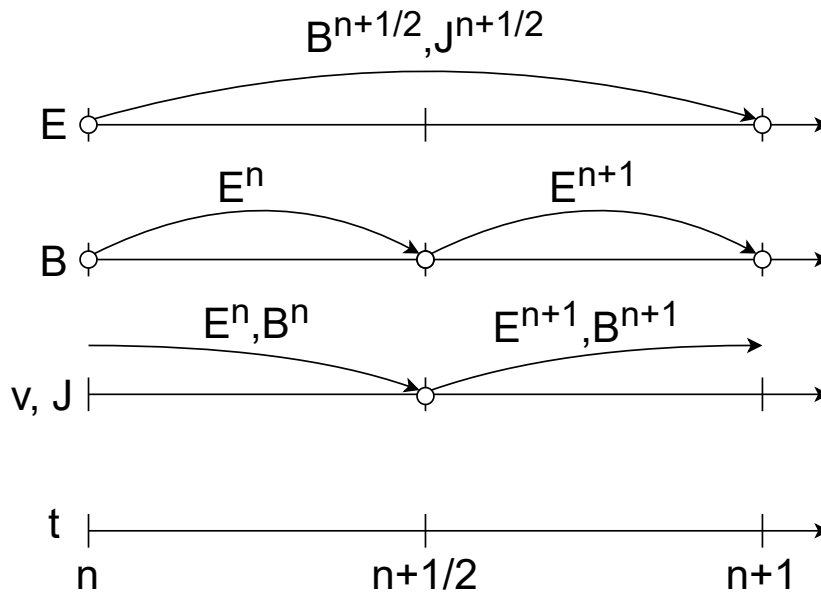


Figure 4: The numerical procedure of the leap frog method. The magnetic field is evolved from the initial value  $B^n$  to  $B^{n+1/2}$  by a half step using  $E^n$ . Then the electric field is taken from  $E^n$  to  $E^{n+1}$  using  $B^{n+1/2}, J^{n+1/2}$ . Lastly, the magnetic field follows from  $B^{n+1/2}$  to  $B^{n+1}$  using  $E^{n+1}$ .

As the name implies, this scheme spreads the macroparticle into a cloud of particles distributed across the cell. The form factor can then be interpreted as the portion of particles that are located near each vertex of the grid cell and “feel” the corresponding field. Higher-order form factors can be used in PIC simulations for better numerical accuracy.

### 4.3 Current deposition

The particles hold charge and their motion creates an electrical current in the grid. Careless deposition of the charge and current creates numerical errors that result in violation of Gauss’s law and phantom forces. While these errors can be corrected with so-called divergence cleaning, it is beneficial to use procedures that conserve the charge and current by design.

My current deposition is derived from a deposition scheme introduced by Esirkepov (2001). The particle motion and form factors are combined in a way that preserves charge and produces the correct total current. The advantage of this method is that it supports all form factors, has good performance, and is suitable for my modification.

As implemented in the ACRONYM code, the scheme takes the macroparticle's positions and velocities at the old and new timestep,  $\vec{x}^n, \vec{x}^{n+1}, \vec{v}^{n-1/2}, \vec{v}^{n+1/2}$ , and calculates the form factors at the positions

$$\begin{aligned} S_i^{old} &= S(|x_i - x^n|), & S_i^{new} &= S(|x_i - x^{n+1}|), \\ S_j^{old} &= S(|y_i - y^n|), & S_j^{new} &= S(|y_i - y^{n+1}|), \\ S_k^{old} &= S(|z_i - z^n|), & S_k^{new} &= S(|z_i - z^{n+1}|), \end{aligned}$$

$$S_i = S_i^{new} - S_i^{old}, \quad S_j = S_j^{new} - S_j^{old}, \quad S_k = S_k^{new} - S_k^{old}.$$

The current introduced by that macroparticle is then given by

$$\begin{aligned} \Delta J_x|_{i,j,k} &= -\frac{Q}{\Delta x^2 \Delta t} \{S_i[(S_j^{old}(S_k^{old} + \frac{1}{2}S_k)] + [S_j(\frac{1}{2}S_k^{old} + \frac{1}{3}S_k)]\}, \\ J_x|_{i,j,k}^{n+1/2} &= \sum_{\alpha=0}^i \Delta J_x|_{\alpha,j,k}, \\ \Delta J_y|_{i,j,k} &= -\frac{Q}{\Delta x^2 \Delta t} \{S_j[(S_i^{old}(S_k^{old} + \frac{1}{2}S_k)] + [S_i(\frac{1}{2}S_k^{old} + \frac{1}{3}S_k)]\}, \\ J_y|_{i,j,k}^{n+1/2} &= \sum_{\alpha=0}^j \Delta J_y|_{i,\alpha,k}, \\ \Delta J_z|_{i,j,k} &= -\frac{Q}{\Delta x^2 \Delta t} \{S_k[(S_i^{old}(S_j^{old} + \frac{1}{2}S_j)] + [S_i(\frac{1}{2}S_j^{old} + \frac{1}{3}S_j)]\}, \\ J_z|_{i,j,k}^{n+1/2} &= \sum_{\alpha=0}^k \Delta J_z|_{i,j,\alpha}, \end{aligned}$$

where  $Q$  is the charge of the macroparticle,  $\Delta x, \Delta t$  are the spatial and temporal resolution of the simulation.

In 2D, the formulas are reduced into

$$\begin{aligned} \Delta J_x|_{i,j} &= -\frac{Q}{\Delta x^2 \Delta t} [S_i(S_j^{old} + \frac{1}{2}S_j)], & J_x|_{i,j}^{n+1/2} &= \sum_{\alpha=0}^i \Delta J_x|_{\alpha,j}, \\ \Delta J_y|_{i,j} &= -\frac{Q}{\Delta x^2 \Delta t} [S_j(S_i^{old} + \frac{1}{2}S_i)], & J_y|_{i,j}^{n+1/2} &= \sum_{\alpha=0}^j \Delta J_y|_{i,\alpha}, \\ J_z|_{i,j}^{n+1/2} &= \frac{Q v_z}{\Delta x^3} (S_i^{old} S_j^{old} + \frac{1}{2}S_i S_j^{old} + \frac{1}{2}S_i^{old} S_j + \frac{1}{3}S_i S_j). \end{aligned}$$

---

In 1D, the formulas are simplified further into

$$\begin{aligned}\Delta J_x|_i &= -\frac{Q}{\Delta x^2 \Delta t} S_i, & J_x|_i^{n+1/2} &= \sum_{\alpha=0}^i \Delta J_x|_\alpha, \\ J_y|_i^{n+1/2} &= \frac{Q v_y}{\Delta x^3} S_i^{new}, & J_z|_i^{n+1/2} &= \frac{Q v_z}{\Delta x^3} S_i^{new}.\end{aligned}$$

My modification of the current deposition is described in the next section.

## Section 5:

# Particle-in-cell equations in curved space-time

This chapter describes modifications of the equations of the PIC procedure to include the effects of curvature of spacetime. The approach follows the 3+1 formalism presented by Komissarov (2004). This formalism greatly simplifies the effort by slicing the 4-dimensional spacetime into 3-dimensional space-like hypersurfaces, which are parametrized by a universal time. This brings two advantages: 1) the equations take on a familiar flat-spacetime form, allowing easier physical interpretation, and 2) the universal time parameter and timestep across the whole grid makes it possible to approach numerically. In this chapter, the speed of light is assumed  $c = 1$ .

### 5.1 Declaration of spacetime

Starting with the general form of the spacetime interval in the Arnowitt–Deser–Misner (ADM) formalism

$$ds^2 = (\beta^2 - \alpha^2)dt^2 + 2\beta_i dx^i dt + \gamma_{ij} dx^i dx^j, \quad (16)$$

we can convert any spacetime metric into a set of parameters and construct a 4-metric in this form

$$g_{\mu\nu} = \begin{pmatrix} \beta^2 - \alpha^2 & \beta_j \\ \beta_i & \gamma_{ij} \end{pmatrix}. \quad (17)$$

where the parameter  $\alpha$  is the lapse function which describes the evolution of time and gives the proper time  $d\tau = \alpha dt$  of the fiducial observer (FIDO), an observer at rest with respect to 3D space, characterized by the 4-velocity  $n_\mu = (-\alpha, 0, 0, 0)$ . The vector  $\beta^i$  is the shift vector, describes the velocity of the reference frame and usually appears in rotating systems such as the Kerr metric. The tensor  $\gamma_{ij}$  is the spatial 3-metric. We see that  $\gamma_{ij} = g_{ij}$ .

Product of the metric and its inverse must give identity  $g_{\mu\sigma} g^{\sigma\nu} = \delta_\mu^\nu$ , leading to:

$$g^{\mu\nu} = \begin{pmatrix} -\frac{1}{\alpha^2} & \frac{\beta^j}{\alpha^2} \\ \frac{\beta^i}{\alpha^2} & \gamma^{ij} - \frac{\beta^i \beta^j}{\alpha^2} \end{pmatrix}. \quad (18)$$

The spatial components of the inverse 4-metric and the inverse 3-metric are generally not equal,  $\gamma^{ij} \neq g^{ij}$ .

## 5.2 Electromagnetic solver

Using the electromagnetic 4-tensor  $F_{\mu\nu}$ , the 3+1 formalism produces the Maxwell's equations in a familiar form, modified by the parameters of the metric

$$\partial_t D^i = \frac{1}{\sqrt{\gamma}} \epsilon^{ijk} \partial_j H_k - 4\pi J^i, \quad (19)$$

$$\partial_t B^i = -\frac{1}{\sqrt{\gamma}} \epsilon^{ijk} \partial_j E_k, \quad (20)$$

$$E_i = \alpha D_i + \sqrt{\gamma} \epsilon_{ijk} \beta^j B^k, \quad (21)$$

$$H_i = \alpha B_i - \sqrt{\gamma} \epsilon_{ijk} \beta^j D^k, \quad (22)$$

where  $\gamma := \det(\gamma_{ij})$  is the determinant of the 3-metric and  $J^i = \alpha j^i - \rho \beta^i$  is the current density measured by the coordinate grid, as obtained during current deposition. The components  $j^i$  are the current density and  $\rho$  is the charge density as measured by the FIDO.

We can express the electric and magnetic fields as  $D^\mu = F^{\mu\nu} n_\nu$  and  $B^\mu = -{}^*F^{\mu\nu} n_\nu$ , which can be interpreted as a projection of the electromagnetic tensor to the reference frame of the FIDO with the 4-velocity  $n_\nu$ , which leads to the identification of  $D^i$  and  $B^i$  as the electromagnetic field measured by the FIDO. The fields  $E_i$  and  $H_i$  are auxiliary fields measured by the reference frame.

Careful examination of the set of equations reveals they are incompatible with the leapfrog scheme. The problem lies in the mixing of electric and magnetic fields  $D^i, B^i$  in the auxiliary fields  $E_i, H_i$  which are used for their time evolution. As described in the previous section, the ordinary procedure would use the initial value  $D^{t_0}$  to take a half step of the magnetic field  $B^{t_0}$  to time  $t_0 + 1/2$ , getting  $B^{t_0+1/2}$ . Then, it would follow with a whole step of the electric field  $D^{t_0}$  to  $D^{t_0+1}$  using the half step value  $B^{t_0+1/2}$ . However, in our case the electric field  $D^{t_0}$  is to be evolved by the auxiliary magnetic field  $H^{t_0+1/2}$  that must be calculated from  $D^{t_0+1/2}$  and  $B^{t_0+1/2}$ . One can also predict that the same problem arises while completing the cycle with the second half step of the magnetic field  $B^{t_0+1/2}$  using  $D^{t_0+1}$ . Solving this problem means modifying the leapfrog scheme.

One solution is to use a predictor-corrector scheme. We start the time evolution procedure with the fields  $D^n, B^n, E^n, H^n$ . After calculating the half step magnetic field  $B^{n+1/2}$ , one makes a prediction of the electric field  $D^{n+1/2}$  by taking a half step using the auxiliary fields  $E^n$  and  $H^n$ . The next step is to calculate the auxiliary fields at the half-step time  $E^{n+1/2}, H^{n+1/2}$  from the half-time step values of  $D^{n+1/2}, B^{n+1/2}$ . Using the half-timestep auxiliary fields we make a correction  $D^{n+1}$ . The same prediction-correction method is then used for the half-step of the magnetic field  $B^{n+1/2}$  to obtain  $B^{n+1}$ .

In my work, this problem is avoided by restricting myself to non-rotating systems where the shift vector  $\beta^i = 0$ . This simplifies the auxiliary fields in equations (21), (22) into the form

$$\begin{aligned} E_i &= \alpha \gamma_{ij} D^j, \\ H_i &= \alpha \gamma_{ij} B^j, \end{aligned}$$

which allows to employ the original leapfrog scheme. There is, however, one remaining catch. If the 3-metric  $\gamma_{ij}$  is not diagonal, the components of the fields mix together. For example, the x-component  $E_x$  would be computed from the components  $D^x, D^y, D^z$ . This causes a problem because they are located at different spots of the grid cell due to the spatial staggering of the Yee lattice and would have a different value at the position of  $E_x$ . This leads to the need for interpolation. This work interpolates the fields using weighted averaging with the weights being the determinant of the 3-metric at the position of the field components. Weighting by the determinant of the metric is computationally cheap while capturing the effect of curvature. In the 1D case, the  $i$ -th grid cell has the  $E_x$  at the position  $i + 1/2$ , denoted as  $E_x|_{i+1/2}$ . Similarly, we have the components  $D^x|_{i+1/2}, D^y|_i, D^z|_i$  and the determinant of the metric at those positions  $\gamma_{i+1/2}, \gamma_i$ . The x-component is already at the right position, but the y- and z-components have to be interpolated like this

$$\begin{aligned} D^y|_{i+1/2} &= \frac{\gamma_i D^y|_i + \gamma_{i+1} D^y|_{i+1}}{\gamma_i + \gamma_{i+1}}, \\ D^z|_{i+1/2} &= \frac{\gamma_i D^z|_i + \gamma_{i+1} D^z|_{i+1}}{\gamma_i + \gamma_{i+1}}. \end{aligned} \tag{23}$$

The interpolation scheme is similar in 2D and 3D. The additional dimensions only extend the spatial staggering and the interpolation is thus calculated from more terms from the surrounding cells

$$\begin{aligned} D^y|_{i+1/2,j} &= (\gamma_{i,j-1/2} D^y|_{i,j-1/2} + \gamma_{i,j+1/2} D^y|_{i,j+1/2} \\ &\quad + \gamma_{i+1,j-1/2} D^y|_{i+1,j-1/2} + \gamma_{i+1,j+1/2} D^y|_{i+1,j+1/2}) \\ &\quad / (\gamma_{i,j-1/2} + \gamma_{i,j+1/2} + \gamma_{i+1,j-1/2} + \gamma_{i+1,j+1/2}). \end{aligned} \tag{24}$$

### 5.3 Particle pusher

The motion of a macroparticle is described by its position  $x^i$ , its coordinate velocity  $v^i$  and its 4-velocity  $u_\mu$ . Borrowing from Crinquant (2021), the equations of motion in the 3+1 formalism come in this form

$$\frac{dx^i}{dt} = v^i = \alpha \frac{\gamma^{ij} u_j}{\Gamma} - \beta^i, \tag{25}$$

$$\begin{aligned} \frac{du_i}{dt} = & \alpha \frac{q}{m} \left( \gamma_{ij} D^j + \sqrt{\gamma} \epsilon_{ijk} \frac{\gamma^{jl} u_l}{\Gamma} B^k \right) \\ & - \Gamma \partial_i \alpha + u_j \partial_i \beta^j - \frac{\alpha}{2\Gamma} \partial_i (\gamma^{jk}) u_j u_k, \end{aligned} \quad (26)$$

where  $\Gamma = \sqrt{1 + \gamma^{ij} u_i u_j}$ . The derivative of the position, in equation (25), is similar to the classical version, in equation (13), the velocity term is multiplied by the parameter  $\alpha$  and the position is also shifted by the shift vector  $\beta^i$ . The acceleration equation (26) has two rows: the first is the Lorentz force multiplied by the parameters of the metric, the second row describes the acceleration caused by the curvature of the spacetime. The first term  $-\Gamma \partial_i \alpha$  can be identified with the gravitational pull of the star, the second  $u_j \partial_i \beta^j$  is tied to the rotation of the system and is interpreted as the centrifugal force, and the third  $-\frac{\alpha}{2\Gamma} \partial_i (\gamma^{jk}) u_j u_k$  diverts the motion of a particle due to the 3-metric gradient.

As in the classical case, the fields located at the grid points need to be interpolated to the position of the particle. For this, the interpolation scheme using the form factors  $S(|x_i - x|)$  can be used. However, the curvature of space needs to be taken into account. The detailed description of the interpolation is covered in Section (6.5).

Because of the non-linear term  $-\frac{\alpha}{2\Gamma} \partial_i (\gamma^{jk}) u_j u_k$ , the Boris push cannot be used to calculate the particle motion. Previous works on GRPIC (Cerutti (2021)) have presented a solution in the form of Strang splitting, where the metric-induced acceleration and the Lorentz force are computed individually. First, the system is transformed by a Lorentz boost into a locally flat spacetime, where the metric terms vanish and the Boris push is suitable and used to calculate the Lorentz portion of the motion, from  $v^i |^{n-1/2}$  to  $\tilde{v}^i |^{n+1/2}$ . After another Lorentz boost back into the original curved space-time, the metric-induced acceleration is applied using an iterative algorithm on  $\tilde{v}^i |^{n+1/2}$  to obtain the final velocity  $v^i |^{n+1/2}$ .

In this work, a different approach is adopted. I modified the Boris push for use in curved spacetime, described in Section 6.4, eliminating the need to transform into a local flat spacetime using the Lorentz boost. However, a method for computing the metric acceleration has not yet been implemented. The code is thus limited to metrics where spacetime is not curved, and the curvature terms vanish. My implementation still allows us to study systems with non-Minkowski metrics.

## Section 6:

# Implementation in the ACRONYM PIC code

This section describes the implementation of curved spacetime modification into the PIC method. ACRONYM (Another Code for pushing Relativistic Objects, Now with Yee lattice and Macro particles) is a PIC simulation code written in C++. It provides simulation in 1D, 2D, or 3D Cartesian cell grid with adjustable spatial and temporal resolution. It offers several options for the electromagnetic field solver, with varying order of accuracy. The particle motion is computed using either the Boris push or the Vay push. It contains many options for the form factors used in the interpolation of the electromagnetic field, in current deposition, and in boundary conditions. MPI parallelization makes it well scalable at high-performance computing systems.

### 6.1 Spacetime curvature

Spacetime in the simulation is characterized by the lapse function array  $\alpha$  and the 3-metric array  $\gamma_{ij}$ . The shift vector  $\beta^i$  has not been included because I initially focused only on non-rotating systems.

Because of the spatial staggering of the fields in the grid, the array  $\alpha$  is separated into two arrays, *alpha\_E* for the electric field and *alpha\_B* for the magnetic field. Each array is further divided into three components corresponding to the three components of the field *alpha\_E[0]* with the value of  $\alpha$  at the position of  $E_x$ , *alpha\_E[1]* for the electric component  $E_y$ , *alpha\_E[2]* for  $E_z$ , and similarly for *alpha\_B*. Each of these components contains a 3D array representing the values across the simulation grid. The same convention is used to introduce arrays *sqrt\_det\_gamma\_E* and *sqrt\_det\_gamma\_B* for the parameter  $\sqrt{\gamma}$ .

Similarly, the 3-metric is separated into two  $3 \times 3$  arrays *gamma\_E* and *gamma\_B* due to the spatial staggering of the Yee lattice. Now, each array has 9 components: the first column contains arrays with values of the 3-metric at the position of the x-component of the field, the second at the position of the y-component, and the third at the position of the z-component. For example, the components *gamma\_E[0,0]*, *gamma\_E[1,0]*, *gamma\_E[2,0]* are three 3D arrays of the size of the simulation containing values of  $\gamma_{00}$ ,  $\gamma_{10}$ ,  $\gamma_{20}$ , respectively, at the grid position of  $E_x$ .

Due to the inconvenience and worse readability of the programming names for the parameters, the mathematical symbols will be used in equations. The reader must bear in mind that the parameters have to be spatially aligned with

the quantities they are being multiplied with.

## 6.2 1D Field solver

The modification of curvature expanded the electromagnetic field. There are now four fields  $D^i, B^i, E_i, H_i$ . The time evolution of the electromagnetic field by done in three steps:

1) a half step of the magnetic field  $B^i$

$$\begin{aligned} B^y|_{i+1/2}^{n+1/2} &= B^y|_{i+1/2}^n + \frac{1}{\sqrt{\gamma}|_{i+1/2}} \frac{E_z|_{i+1}^n - E_z|_i^n}{\Delta x} \frac{\Delta t}{2}, \\ B^z|_{i+1/2}^{n+1/2} &= B^z|_{i+1/2}^n - \frac{1}{\sqrt{\gamma}|_{i+1/2}} \frac{E_y|_{i+1}^n - E_y|_i^n}{\Delta x} \frac{\Delta t}{2}, \end{aligned}$$

2) whole step of the electric field  $D^i$

$$\begin{aligned} D^x|_{i+1/2}^{n+1} &= D^x|_{i+1/2}^n - J^x|_{i+1/2}^{n+1/2} \Delta t, \\ D^y|_i^{n+1} &= D^y|_i^n - J^y|_i^{n+1/2} \Delta t + \frac{1}{\sqrt{\gamma}|_i} \frac{H_z|_{i-1/2}^{n+1/2} - H_z|_{i+1/2}^{n+1/2}}{\Delta x} \Delta t, \\ D^z|_i^{n+1} &= D^z|_i^n - J^z|_i^{n+1/2} \Delta t - \frac{1}{\sqrt{\gamma}|_i} \frac{H_y|_{i-1/2}^{n+1/2} - H_y|_{i+1/2}^{n+1/2}}{\Delta x} \Delta t, \end{aligned}$$

3) second half step of the magnetic field  $B^i$ .

$$\begin{aligned} B^y|_{i+1/2}^{n+1} &= B^y|_{i+1/2}^{n+1/2} + \frac{1}{\sqrt{\gamma}|_{i+1/2}} \frac{E_z|_{i+1}^{n+1} - E_z|_i^{n+1}}{\Delta x} \frac{\Delta t}{2}, \\ B^z|_{i+1/2}^{n+1} &= B^z|_{i+1/2}^{n+1/2} - \frac{1}{\sqrt{\gamma}|_{i+1/2}} \frac{E_y|_{i+1}^{n+1} - E_y|_i^{n+1}}{\Delta x} \frac{\Delta t}{2}, \end{aligned}$$

Each of these steps is preceded by the computation of the auxiliary fields  $H_i, E_i$  from the fields  $B^i, D^i$ , respectively

$$\begin{aligned} E_i &= \alpha \gamma_{ij} D^j, \\ H_i &= \alpha \gamma_{ij} B^j. \end{aligned}$$

For a system with a diagonal 3-metric  $\gamma_{ij}$  this is straightforward, the components  $D^i, B^i$  do not mix, are aligned with  $E_i, H_i$  and no interpolation is needed. As described in section 5.2, introducing a non-diagonal 3-metric  $\gamma_{ij}$  complicates the

computation, because the field components mix and are misaligned in the Yee lattice. This requires interpolation according to equations (23).

To test the correct functionality of the field solver, vacuum simulations were run in which a sine wave in  $D^y$  was generated at a single point of the domain. The boundary conditions were set to absorb the electromagnetic field at the boundaries. The propagation of the wave was investigated to detect numerical errors, and the propagation speed was calculated and compared to the expected analytical value in various configurations of spacetime. The propagation of the wave was first simulated in the Minkowski spacetime, where the behaviour is expected not to change with respect to the unmodified code. The result of the simulation is in Figure (5) on the left. No obvious errors in the propagation were found. The propagation speed measured from the simulation agreed with the speed of light in vacuum, which is also obvious from the figure. The units of the axis are such that a displacement of  $1dx/d_e$  in time  $1dt\omega_p$  corresponds to the speed of light.

Then, a non-trivial metric was introduced. In Cartesian coordinates the Schwarzschild spacetime interval reads

$$ds^2 = -\frac{(1-\xi)^2}{(1+\xi)^2}dt^2 + (1+\xi)^4 dx^i dx_i, \quad \xi < 1,$$

$$\xi = \frac{R_S}{4R}, \quad R_S = \frac{2GM}{c^2}, \quad R = \sqrt{x^2 + y^2 + z^2}.$$

Comparing with the general ADM form of the spacetime interval

$$ds^2 = (\beta^2 - \alpha^2)dt^2 + 2\beta_i dx^i dt + \gamma_{ij} dx^i dx^j, \quad (27)$$

we get the parameters of the metric

$$\alpha = \frac{1-\xi}{1+\xi}, \quad \gamma_{ij} = \begin{cases} (1+\xi)^4 & \text{for } i = j, \\ 0 & \text{for } i \neq j. \end{cases}$$

First, the metric was set to be constant across the simulation domain with the values of the Schwarzschild metric at  $R = 2R_S$ ,  $\alpha(R = 2R_S) \approx 0.78$ ,  $\gamma_{ii}(R = 2R_S) \approx 1.6$  to check for stability and propagation speed. This radius was chosen because for a compact object of mass  $M = 2M_\odot$ ,  $2R_S \approx 11\text{km}$ , which corresponds to a radius just above the surface of a neutron star. With this configuration, I experienced a problem with boundary conditions, which are designed to react to the incoming electromagnetic field and damp it down according to the unmodified Maxwell's equations, not accounting for the curvature. When the electromagnetic wave arrives at the boundary, the damping is calculated incorrectly, a jump in the electromagnetic field is created that diverges into infinity and propagates back into the simulation, numerically ruining it. To solve this issue, the metric was

padding near the boundaries to approach the Minkowski metric. This padding was done through a linear interpolation between the Minkowski metric and the value of the metric at the border of the padding. The result of the simulation is on the right side of Figure (5). The propagation speed was measured to agree with the analytical value, calculated from the Maxwell's equations in 3+1 formalism, with the assumption of a diagonal constant metric  $\gamma_{ij} = 0$  for  $i \neq j$ ,  $\partial_i \alpha = 0$ ,  $\partial_i \gamma_{ij} = 0$

$$\begin{aligned} E_i &= \alpha \gamma_{ii} D^i \Rightarrow \nabla \times E_i = \alpha \gamma_{ii} \nabla \times D^i, \\ H_i &= \alpha \gamma_{ii} B^i \Rightarrow \nabla \times H_i = \alpha \gamma_{ii} \nabla \times B^i, \\ \partial_t D^y &= \frac{1}{\sqrt{\gamma}} \nabla \times H_z = \frac{1}{\sqrt{\gamma}} \alpha \gamma_{zz} \nabla \times B^z, \\ \partial_t B^z &= -\frac{1}{\sqrt{\gamma}} \nabla \times E_y = -\frac{1}{\sqrt{\gamma}} \alpha \gamma_{yy} \nabla \times D^y, \\ \partial_t^2 D^y &= \frac{\alpha^2 \gamma_{yy}^2}{\gamma} \nabla^2 D^y, \\ v_p &\propto \frac{\alpha \gamma_{yy}}{\sqrt{\gamma}}. \end{aligned}$$

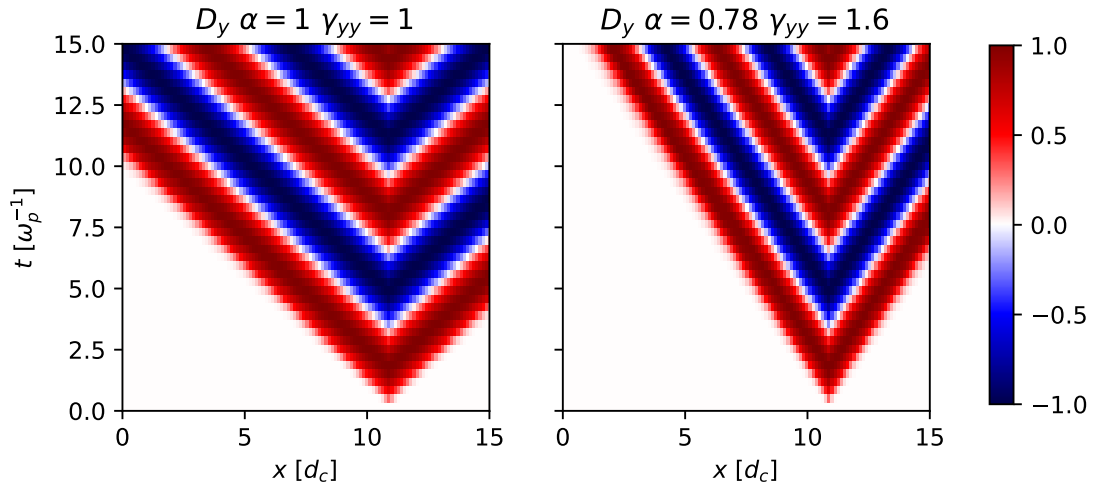


Figure 5: The electric field  $D^y$  in the 1D simulation of the electromagnetic wave propagating in the x-direction. Left: Minkowski metric, the propagation is unchanged from the unmodified code. Right: Constant metric with values corresponding to the Schwarzschild metric at  $R = 2R_S$ .

Second, the metric was set to curve according to the Schwarzschild metric in the distance range of 2-5 Schwarzschild radii. This was done to check stability of the wave propagation through curved spacetime. The propagation speed was measured at various positions of the simulation, which agreed with the predicted speed calculated from the parameter of the metric at that position, shown in Figure 6.

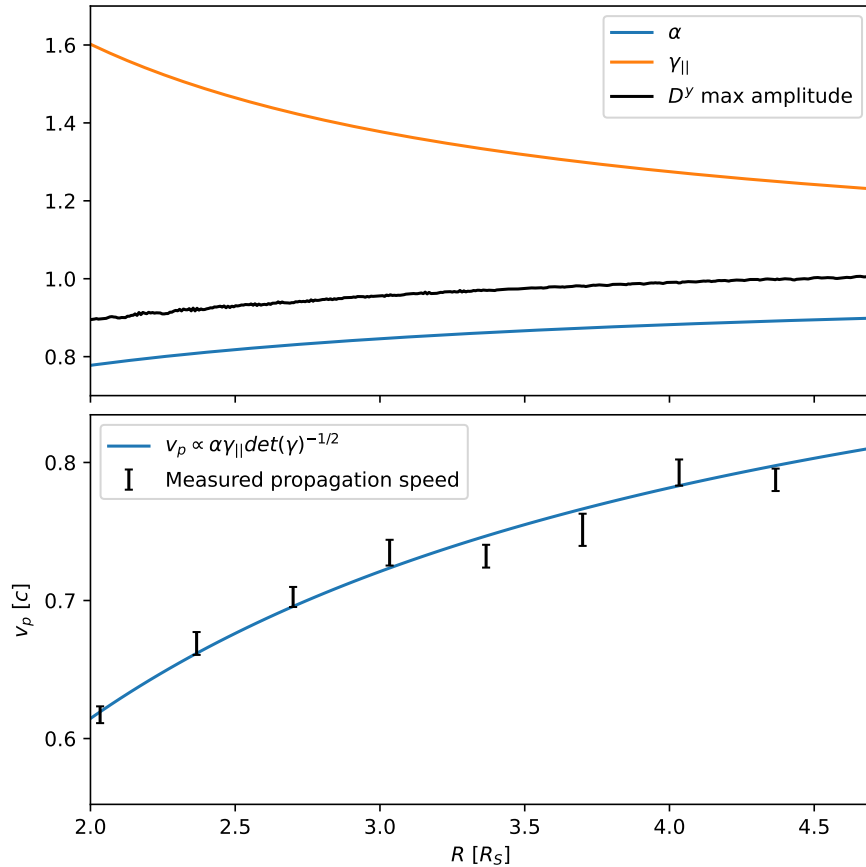


Figure 6: Top: Parameters of the metric in relation to the position in the simulation, that corresponds to a radius in the Schwarzschild metric. The maximum amplitude of the wave, in black, changes as it travels through the curved spacetime. Bottom: The measured propagation speed of the wave in black. The blue line describes the predicted propagation speed calculated from the parameters of the metric

### 6.3 2D Field solver

The underlying method is the same as in the 1D case. The additional dimension introduces more terms into the time evolution:

1) a half step of the magnetic field  $B^i$

$$\begin{aligned}
 B^x|_{i,j+1/2}^{n+1/2} &= B^x|_{i,j+1/2}^n - \frac{1}{\sqrt{\gamma}|_{i,j+1/2}} \frac{E_z|_{i,j+1}^n - E_z|_{i,j}^n}{\Delta x} \frac{\Delta t}{2}, \\
 B^y|_{i+1/2,j}^{n+1/2} &= B^y|_{i+1/2,j}^n + \frac{1}{\sqrt{\gamma}|_{i+1/2,j}} \frac{E_z|_{i+1,j}^n - E_z|_{i,j}^n}{\Delta x} \frac{\Delta t}{2}, \\
 B^z|_{i+1/2,j+1/2}^{n+1/2} &= B^z|_{i+1/2,j+1/2}^n - \frac{1}{\sqrt{\gamma}|_{i+1/2,j+1/2}} \\
 &\quad \frac{E_y|_{i+1,j+1/2}^n - E_y|_{i,j+1/2}^n + E_x|_{i+1/2,j+1}^n - E_x|_{i+1/2,j}^n}{\Delta x} \frac{\Delta t}{2},
 \end{aligned}$$

2) whole step of the electric field  $D^i$

$$\begin{aligned}
 D^x|_{i+1/2,j}^{n+1} &= D^x|_{i+1/2,j}^n - J^x|_{i+1/2,j}^{n+1/2} \Delta t \\
 &\quad - \frac{1}{\sqrt{\gamma}|_{i+1/2,j}} \frac{H_z|_{i+1/2,j-1/2}^{n+1/2} - H_z|_{i+1/2,j+1/2}^{n+1/2}}{\Delta x} \Delta t, \\
 D^y|_{i,j+1/2}^{n+1} &= D^y|_{i,j+1/2}^n - J^y|_{i,j+1/2}^{n+1/2} \Delta t \\
 &\quad + \frac{1}{\sqrt{\gamma}|_{i,j+1/2}} \frac{H_z|_{i-1/2,j+1/2}^{n+1/2} - H_z|_{i+1/2,j+1/2}^{n+1/2}}{\Delta x} \Delta t, \\
 D^z|_{i,j}^{n+1} &= D^z|_{i,j}^n - J^z|_{i,j}^{n+1/2} \Delta t \\
 &\quad - \frac{1}{\sqrt{\gamma}} \frac{H_y|_{i-1/2,j}^{n+1/2} - H_y|_{i+1/2,j}^{n+1/2} - H_x|_{i,j-1/2,k}^{n+1/2} + H_x|_{i,j+1/2}^{n+1/2}}{\Delta x} \Delta t,
 \end{aligned}$$

3) second half step of the magnetic field  $B^i$ .

$$\begin{aligned}
 B^x|_{i,j+1/2}^{n+1} &= B^x|_{i,j+1/2}^{n+1/2} - \frac{1}{\sqrt{\gamma}|_{i,j+1/2}} \frac{E_z|_{i,j+1}^{n+1} - E_z|_{i,j}^{n+1}}{\Delta x} \frac{\Delta t}{2}, \\
 B^y|_{i+1/2,j}^{n+1} &= B^y|_{i+1/2,j}^{n+1/2} + \frac{1}{\sqrt{\gamma}|_{i+1/2,j}} \frac{E_z|_{i+1,j}^{n+1} - E_z|_{i,j}^{n+1}}{\Delta x} \frac{\Delta t}{2}, \\
 B^z|_{i+1/2,j+1/2}^{n+1} &= B^z|_{i+1/2,j+1/2}^{n+1/2} - \frac{1}{\sqrt{\gamma}|_{i+1/2,j+1/2}} \\
 &\quad \frac{E_y|_{i+1,j+1/2}^{n+1} - E_y|_{i,j+1/2}^{n+1} + E_x|_{i+1/2,j+1}^{n+1} - E_x|_{i+1/2,j}^{n+1}}{\Delta x} \frac{\Delta t}{2}.
 \end{aligned}$$

The computation of the auxiliary fields  $E_i, H_i$  is the same as in the 1D case. In the case of non-diagonal 3-metrics, the interpolation is more complicated because of the spatial staggering of the Yee lattice and is calculated through equation (24).

The 2D field solver was tested in a manner similar to the 1D implementation. I ran 2D simulations with a sine wave in  $D^z$  generated in the centre of the simulation grid. This wave then propagated outward. This was done for the Minkowski metric, for a constant isotropic metric with values of the Schwarzschild metric at  $R = 2R_S$ , and for a constant anisotropic metric  $\alpha = 1, \gamma_{xx} = 4, \gamma_{yy} = \gamma_{zz} = 1$ . Figure (7) shows the comparison of the electromagnetic fields in the Minkowski metric and the Schwarzschild metric. The wave in electric field  $D^z$  is monopolar, while the magnetic field is dipolar. The wave is stable and propagates isotropically. It is visible that the propagation speed is reduced by the change in the metric parameters. Figure (8) contains the comparison of the wave in Minkowski metric and the constant anisotropic metric. Because the space is stretched in the x-direction, propagation in the x-direction is slower than in the y-direction, and the wave looks squished. The propagation speed in the y-direction is identical to that in Minkowski spacetime. The two components of the magnetic field also differ in amplitude, the colours in the plots of  $B^y$  are brighter than the fainter  $B^x$ .

## 6.4 Modified Boris push

By introducing the quantities  $\tilde{D}_i = \alpha\gamma_{ij}D^j, \tilde{B}^i = \alpha\sqrt{\gamma}B^i$  and omitting the metric-induced terms the equation of acceleration (26) takes the familiar form

$$\frac{du_i}{dt} = \frac{q}{m} \left( \tilde{D}_i + \epsilon_{ijk} \frac{\gamma^{jl}u_l}{\Gamma} \tilde{B}^k \right). \quad (28)$$

With great care for the position of the indices, the Boris push can be rewritten to calculate the contribution of the Lorenz force in curved spacetime

$$\begin{aligned} u_i^- &= u_i^{n-1/2} + \frac{q\tilde{D}_i}{2m} \Delta t, \\ f_1^i &= \frac{q\Delta t}{2m\Gamma} \tilde{B}^i, & f_2^i &= \frac{2f_1^i}{1 + (f_1^i)^2}, \\ u_i' &= u_i^- + \epsilon_{ijk} \gamma^{jl} u_l^- f_1^k, & u_i^+ &= u_i^- + \epsilon_{ijk} \gamma^{jl} u_l' f_2^k, \\ u_i^{n+1/2} &= u_i^+ + \frac{q\tilde{D}_i}{2m} \Delta t, \end{aligned}$$

where  $\Gamma = \sqrt{1 + \gamma^{ij}u_i u_j}$ . The calculated velocity is used to update the position of the particle

$$x^i|^{n+1} = x^i|^{n+1/2} + \alpha \frac{\gamma^{ij}u_j}{\Gamma} \Delta t.$$

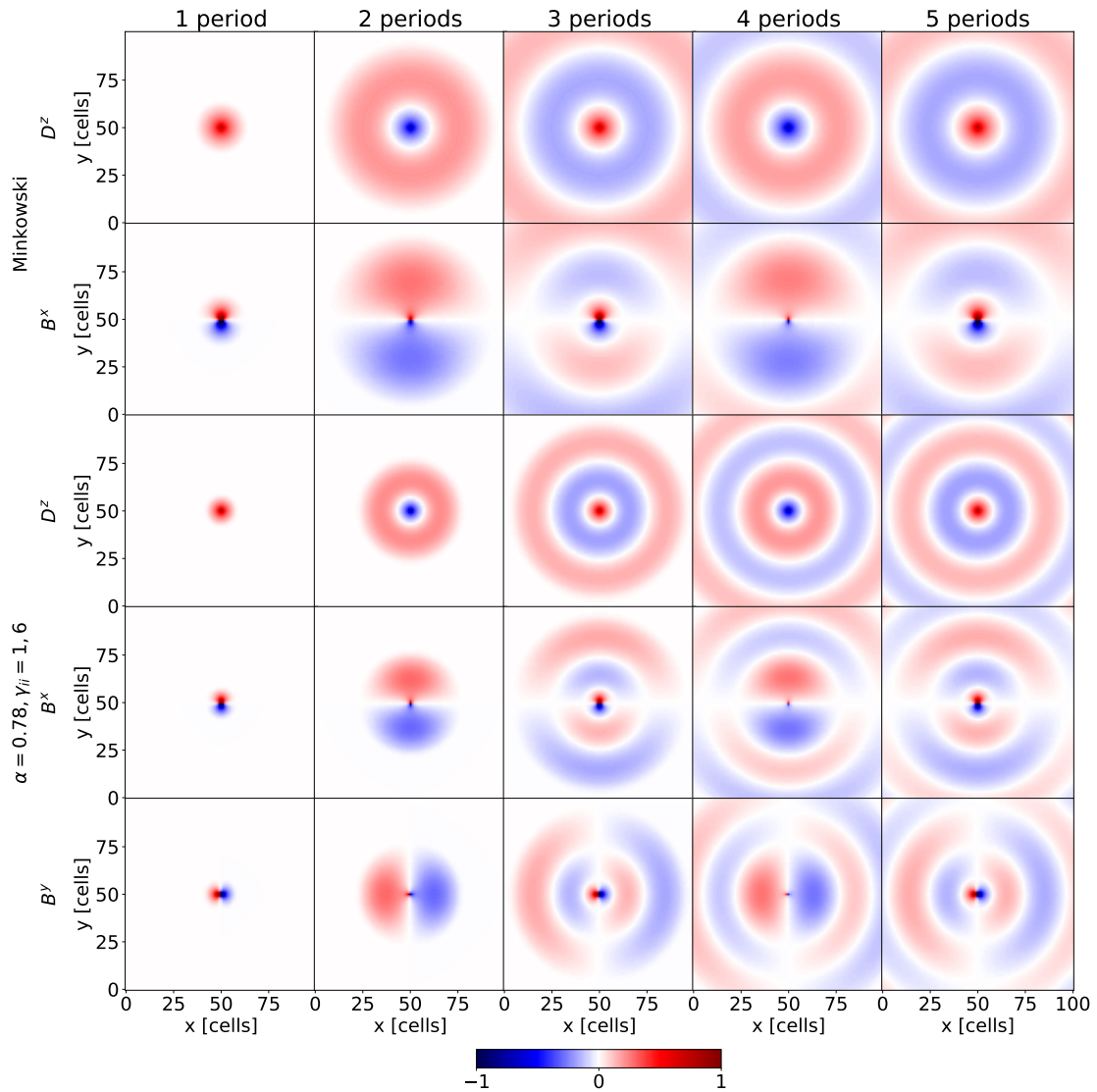


Figure 7: Propagation of a sine wave generated in  $D^z$  at the centre of a 2D simulation. Horizontal axis shows x-direction, vertical axis is y-direction, the colour in the plot represents the strength of the field, red means positive values, blue negative. By rows: 1) electric field  $D^z$  in Minkowski metric 2) magnetic field  $B^x$  in Minkowski metric 3) electric field  $D^z$  in a constant metric with values of Schwarzschild metric at  $R = 2R_S$ , 4) magnetic field  $B^x$  in a constant metric, 5) magnetic field  $B^y$  in a constant metric.

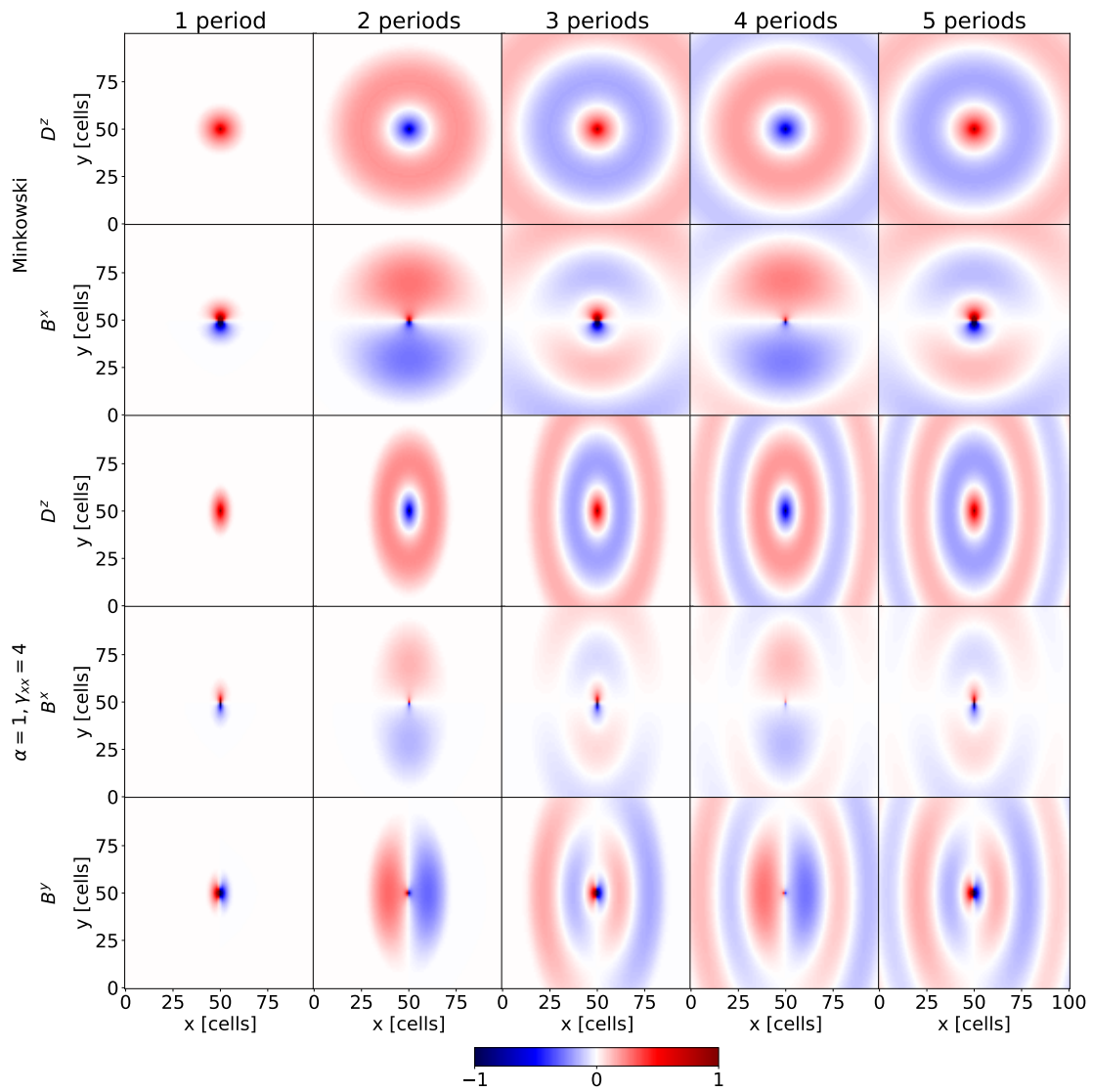


Figure 8: The same as in Figure (7), but the constant Schwarzschild metric is replaced by an artificial constant metric  $\alpha = 1, \gamma_{xx} = 4, \gamma_{yy} = \gamma_{zz} = 1$

## 6.5 Field-particle interpolation

This part addresses the interpolation of the electromagnetic fields  $D^i, B^i$  and the parameters of the metric  $\alpha, \gamma_{ij}, \gamma^{ij}$  to the position of a macroparticle used in the computation of the particle motion. My method uses the form factors  $S(|x_i - x|)$ . To include the curvature of space, the weight of a grid point is multiplied by the value of the determinant of the 3-metric  $\gamma = \det(\gamma_{ij})$  at that point. However, since the determinant depends on the position, the form factors in different directions cannot be isolated and then simply multiplied during field interpolation, as in equation (15). A matrix has to be constructed that combines the form factors in each direction from the beginning. The size of the form matrix depends on the chosen form factor, as different schemes use a different number of nearby cells to interpolate. To normalise the form matrix to one, the individual components of the form matrix have to be divided by the overall sum

$$S_{i,j}(x, y) = \frac{\gamma_{i,j} S(|x_i - x|) S(|y_j - y|)}{\sum_{i,j} \gamma_{i,j} S(|x_i - x|) S(|y_j - y|)}.$$

To save space and increase readability, the coordinates and normalisation will not be included from now on.

In the case of 1D interpolation, the spatial staggering of the Yee lattice produces only two such 1D form “matrices”, one for fields at the grid point ( $D^y, D^z, B^x$ ) and one for fields in between grid points  $D^x, B^y, B^z$ .

$$\begin{aligned} S_i(x) &= \gamma_i S(|x_i - x|), \\ S_{i+1/2}(x) &= \gamma_{i+1/2} S(|x_{i+1/2} - x|). \end{aligned}$$

Introducing another dimension to 2D adds additional staggering, resulting in the need for two more form matrices.

$$\begin{aligned} S_{i,j}(x, y) &= \gamma_{i,j} S(|x_i - x|) S(|y_j - y|), \\ S_{i+1/2,j}(x, y) &= \gamma_{i+1/2,j} S(|x_{i+1/2} - x|) S(|y_j - y|), \\ S_{i,j+1/2}(x, y) &= \gamma_{i,j+1/2} S(|x_i - x|) S(|y_{j+1/2} - y|), \\ S_{i+1/2,j+1/2}(x, y) &= \gamma_{i+1/2,j+1/2} S(|x_{i+1/2} - x|) S(|y_{j+1/2} - y|). \end{aligned}$$

The electromagnetic field and the parameters of the metric are then interpolated

in this manner

$$\begin{aligned}
D_k &= S_{i+1/2,j} \gamma_{kx} |_{i+1/2,j} D^x |_{i+1/2,j} \\
&\quad + S_{i,j+1/2} \gamma_{ky} |_{i,j+1/2} D^y |_{i,j+1/2} \\
&\quad + S_{i,j} \gamma_{kz} |_{i,j} D^z |_{i,j}, \\
\gamma_{kx} &= S_{i+1/2,j} \gamma_{kx} |_{i+1/2,j}, \\
\gamma_{ky} &= S_{i,j+1/2} \gamma_{ky} |_{i,j+1/2}, \\
\gamma_{kz} &= S_{i,j} \gamma_{kz} |_{i,j}, \\
\alpha &= S_{i+1/2,j} \alpha |_{i+1/2,j}, \\
B^x &= S_{i,j+1/2} \sqrt{\gamma} |_{i,j+1/2} B^x |_{i,j+1/2}, \\
B^y &= S_{i+1/2,j} \sqrt{\gamma} |_{i+1/2,j} B^y |_{i+1/2,j}, \\
B^z &= S_{i+1/2,j+1/2} \sqrt{\gamma} |_{i+1/2,j+1/2} B^z |_{i+1/2,j+1/2},
\end{aligned}$$

that is similar for both 1D and 2D, differing only in the form matrices and number of indices. The inverse 3-metric shares identical interpolation with the 3-metric and thus was omitted. Multiplication by the 3-metric  $\gamma_{ij}$  in interpolation of  $D^i$  and by the square root of the 3-metric determinant  $\sqrt{\gamma}$  in interpolation of  $B^i$  is done for a very good reason. Multiplying by the interpolated parameter  $\alpha$  we get the quantities

$$\begin{aligned}
\tilde{D}_k &= \alpha D_k, \\
\tilde{B}^k &= \alpha B^k,
\end{aligned}$$

that are ready to be used in the modified Boris push. This way, the number of calculations is reduced and the need to interpolate  $\sqrt{\gamma}$  is completely eliminated, compared to the case where  $D^k, B^k, \gamma_{kl}$  and  $\sqrt{\gamma}$  are interpolated separately and later combined for the computation of  $\tilde{B}^k$

## 6.6 Novel approach to current deposition

My current deposition scheme keeps the idea of the Esirkepov deposition scheme. Similarly to the interpolation of the fields to the location of the particle, the form factors are multiplied by the determinant of the 3-metric to include the effect of curvature. The determinant is dependent on the position in the grid, which prevents us from constructing the form factors in the coordinate directions independently and combining them in the computation of the current. A matrix is constructed in which the form factors in different directions are combined and multiplied by the corresponding 3-metric determinant. To preserve charge conservation, the resulting form matrices have to copy the ratios of the form factors as presented in

the Esirkepov deposition. The components of the form matrix are also divided by its sum to keep it normalised to one. The normalisation is left out of the equations to improve readability.

The modification of the 1D current deposition is simple, actually.

$$S_i^{old} = \gamma_i S(|x_i - x^n|), \quad S_i^{new} = \gamma_i S(|x_i - x^{n+1}|),$$

$$S_i = S_i^{new} - S_i^{old},$$

$$\Delta J^x|_i = -\frac{Q}{\Delta x^2 \Delta t} S_i, \quad J^x|_{i+1/2}^{n+1/2} = \sum_{\alpha=0}^i \Delta J^x|_{\alpha},$$

$$J^y|_i^{n+1/2} = \frac{Q v^y}{\Delta x^3} S_i^{new}, \quad J^z|_i^{n+1/2} = \frac{Q v^z}{\Delta x^3} S_i^{new},$$

where the positions and velocities are calculated using the modified Boris push.

In the 2D case, ratios of the form factors give us

$$X_{i,j}^{old} = \gamma_{i+1/2,j} S(|x_i - x^n|) \frac{S(|y_j - y^n|) + S(|y_j - y^{n+1}|)}{2},$$

$$X_{i,j}^{new} = \gamma_{i+1/2,j} S(|x_i - x^{n+1}|) \frac{S(|y_j - y^n|) + S(|y_j - y^{n+1}|)}{2},$$

$$Y_{i,j}^{old} = \gamma_{i,j+1/2} S(|y_j - y^n|) \frac{S(|x_i - x^n|) + S(|x_i - x^{n+1}|)}{2},$$

$$Y_{i,j}^{new} = \gamma_{i,j+1/2} S(|y_j - y^{n+1}|) \frac{S(|x_i - x^n|) + S(|x_i - x^{n+1}|)}{2},$$

$$X_{i,j} = X_{i,j}^{new} - X_{i,j}^{old},$$

$$Y_{i,j} = Y_{i,j}^{new} - Y_{i,j}^{old},$$

$$Z_{i,j} = \gamma_{i,j} \left[ \frac{S(|x_i - x^n|)S(|y_j - y^n|) + S(|x_i - x^{n+1}|)S(|y_j - y^{n+1}|)}{3} + \frac{S(|x_i - x^n|)S(|y_j - y^{n+1}|) + S(|x_i - x^{n+1}|)S(|y_j - y^n|)}{6} \right].$$

The matrices have important properties: summing over the index  $i$  and  $j$  in the form matrices  $X_{i,j}$  and  $Y_{i,j}$ , respectively, results in a sum of zero, and summing over the whole form matrix  $Z_{i,j}$  gives a sum of one. This ensures that the current

deposited conserves the total charge. The current is then calculated as

$$\begin{aligned}\Delta J^x|_{i,j} &= -\frac{Q}{\Delta x^2 \Delta t} X_{i,j}, & J^x|_{i+1/2,j} &= \sum_{\alpha=0}^i \Delta J^x|_{\alpha,j}, \\ \Delta J^y|_{i,j} &= -\frac{Q}{\Delta x^2 \Delta t} Y_{i,j}, & J^y|_{i,j+1/2} &= \sum_{\alpha=0}^j \Delta J^y|_{i,\alpha}, \\ J^z|_{i,j} &= \frac{Q v^z}{\Delta x^3} Z_{i,j}.\end{aligned}$$

This method allows us to compute **charge-conserving current deposition** in any non-rotating curved spacetime using any form factor.

## Section 7:

### Plasma simulations

In this chapter, the modified code is used for simulations of thermal plasma. The electric and magnetic fields are investigated and compared to a reference simulation. The energy of different components of the simulation is studied to check for energy conservation. A Fourier analysis is performed to obtain dispersion relations of plasma oscillations and electromagnetic waves present in the simulated plasma. The speed of light  $c = 1$  in the whole chapter.

#### 7.1 1D Thermal plasma

I ran a set of 1D simulations with a plasma consisting of electrons and positrons with a Maxwellian velocity distribution with thermal velocity  $v_{th} = 0.1c$  and a density of 40 particles per cell (ppc). No external magnetic field was present. The simulations were run for 20000 timesteps with a temporal resolution normalised to the plasma frequency  $\Delta t \omega_p = 0.014$ , which gives approximately  $20000 \Delta t \omega_p = 280$  plasma oscillations. The grid consisted of 2000 cells in the x-direction with a spatial resolution  $\Delta x/d_c = 0.047$ , where  $d_c = c/\omega_p$  represents the skin depth, the distance light travels in one plasma oscillation. This means that  $(\Delta x/d_c)^{-1} \approx 21$  is the number of cells light travels through during one plasma oscillation. Then  $280/(20000/21) = 2.94$  tells us that light has enough time to travel through the entire simulation three times, which means that distant locations in the simulation received information about each other and the plasma is in equilibrium state. Dividing the temporal and spatial resolution  $\Delta t c/\Delta x = 0.3$  gives us the Courant number well below the Courant–Friedrichs–Lewy (CFL) condition limit, which ensures numerical stability of the field solver. The boundary condition was set to periodic, meaning that the simulation wraps around the boundaries.

In this section, three simulations are presented: 1) a reference simulation made with unmodified code (no GR), 2) a simulation run with the Minkowski metric  $\alpha = 1, \gamma_{ii} = 1$  (Minkowski), which, in principle, should be identical to the reference one, and 3) a simulation with a metric that is constant across the simulation and whose values correspond to the values of the Schwarzschild metric at  $R = 2R_S$ ,  $\alpha = 0.78, \gamma_{ii} = 1.6$ .

Figure (9) shows the electric fields in the three simulations. The electrons and positrons oscillate in all directions, performing plasma oscillations and generating electromagnetic waves. Plasma oscillations are longitudinal and can propagate as Langmuir electrostatic waves only in the x-direction, which are visible in the x-component of the electric field  $D^x$ . Electromagnetic waves are transversal waves

and propagate in the perpendicular direction. Thus, they only appear in the  $y$ - and  $z$ -component of the electromagnetic field  $D^y, D^z, B^y, B^z$ . The field strength range of the color scale is similar in all three simulations. The reference simulation and the Minkowski simulation are almost the same, as expected, with subtle differences that arise from the modified equations that can be attributed to numerical noise.

The propagation speed of the electromagnetic waves can be quickly approximated from the slope of the lines in the figure. The units of the axes have the property that a displacement of  $1 d_c$  in time  $1 \omega_p$  gives a propagation speed equal to the speed of light. Then, if the horizontal and vertical axes have equal aspect and a wave is a diagonal line, it is propagating at the speed of light, which can be seen in the electric field  $D^y, D^z$  in the reference and Minkowski simulations. If the slope of the lines is steeper than diagonal, then the wave has a lower propagation speed than the speed of light, as seen in the Schwarzschild simulation.

The magnetic field components are shown in Figure (10). The  $B^x$  component is zero, because the plasma oscillations are purely electrostatic, and the electromagnetic waves appear only in the components  $B^y$  and  $B^z$ . Again, the range of the field strength is similar for all three cases. Subtle differences in field strength are visible between the reference and Minkowski simulations, with the propagation speed at the speed of light. The lower propagation speed in the Schwarzschild metric is present also in the magnetic field.

The simulation also outputs the total energy of the simulation and energy of various components of the electric and magnetic field as well as the energy of particles. The energy of the components of the electric and the magnetic field is calculated using equations

$$E_D^i = \frac{\Delta x^3}{8\pi} \sum_{j,k,l} (D^i|_{j,k,l})^2,$$

$$E_B^i = \frac{\Delta x^3}{8\pi} \sum_{j,k,l} (B^i|_{j,k,l})^2.$$

The total energy of the fields is the sum of its components

$$E_D = \sum_{i=0}^3 E_D^i,$$

$$E_B = \sum_{i=0}^3 E_B^i.$$

---

The energy of each particle is calculated through the relativistic equation

$$K_i = (\Gamma_i - 1) m_i c^2,$$

where  $\Gamma_i$  is the Lorentz factor,  $m_i$  is the mass of the macroparticle and  $c$  is the speed of light. The total energy is the sum of the field energies and the particle kinetic energy

$$E_{tot} = E_D + E_B + K.$$

Figure (11) shows the total energy  $E$ , the energy of the electric  $E_D$  and magnetic field  $E_B$ , the energy of particles  $K$  and the divergence of  $B^i$  for the three simulations. All energies were normalised to the initial kinetic energy of particles. At the start of the simulation, the particles need a bit of time to generate the electromagnetic field and establish the plasma environment, which causes a jump in total energy. The first 500 timesteps have been cut off in the figures to remove the initial jump and improve readability. The total energy has a very slow linear growth of about 0.02 % over the time of the simulation in all reference, Minkowski, and Schwarzschild cases. The energies in the reference and Minkowski simulations are very similar. An increase in the magnetic field energy and a decrease in the energy of particles is seen in the Schwarzschild simulation. The divergence remains zero throughout the simulation. Figure (12) shows the energy of the components of the electric and magnetic field. The energy in  $D^x$  does not change with the metric parameters, while the components connected to the electromagnetic waves have an increased energy in the Schwarzschild simulation. This implies that during the generation of the fields at the start of the simulation, the electromagnetic waves gain more energy at the expense of the particles in the Schwarzschild case than in the reference or Minkowski case.

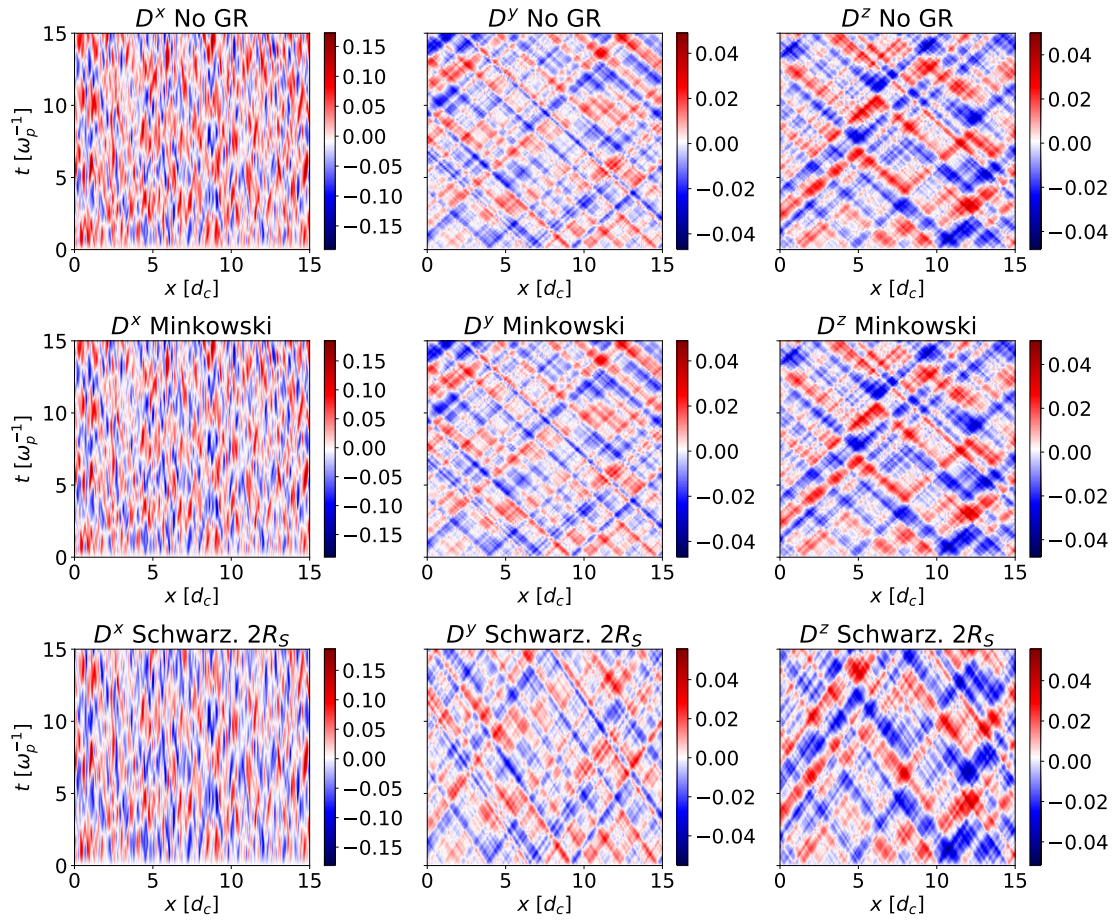


Figure 9: Electric fields in the three 1D plasma simulations. The vertical axis is the simulation time, the horizontal axis is the position, the colour represents the field strength.

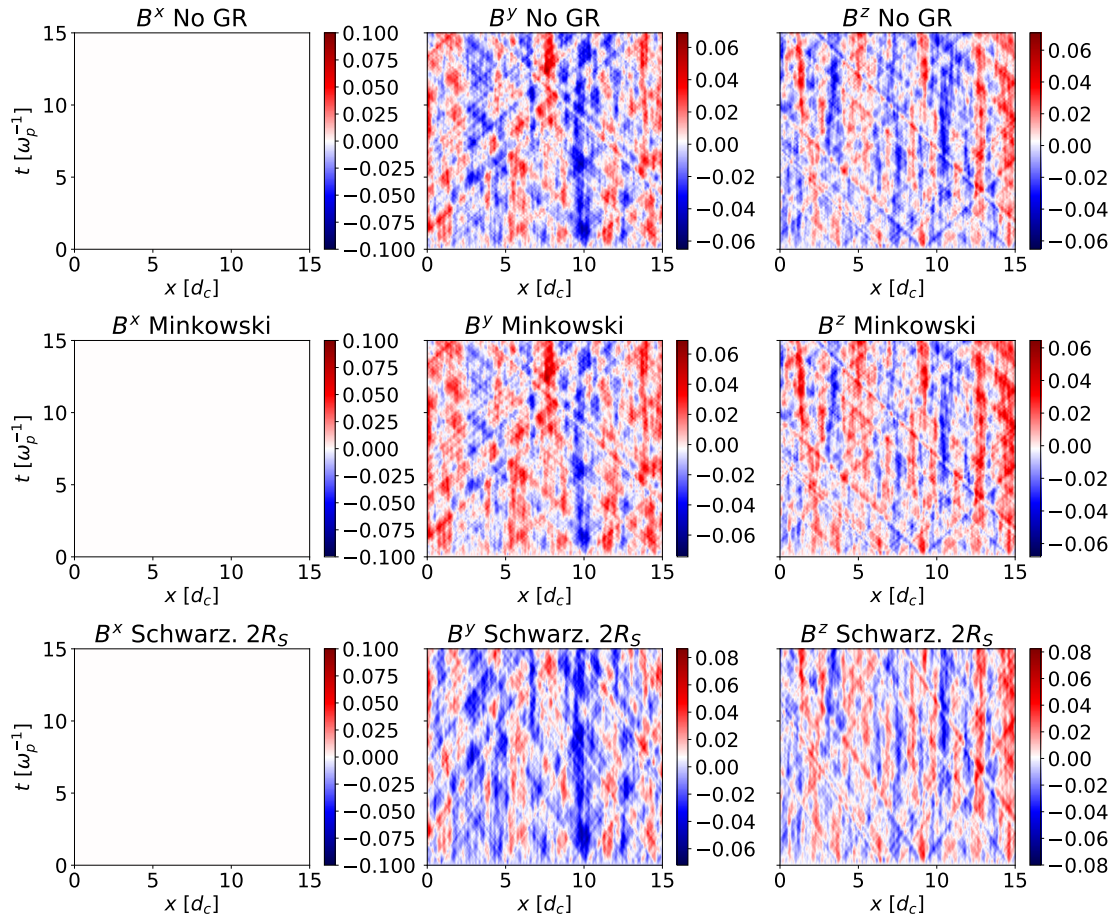


Figure 10: The same like in Figure (9), but for magnetic field components.

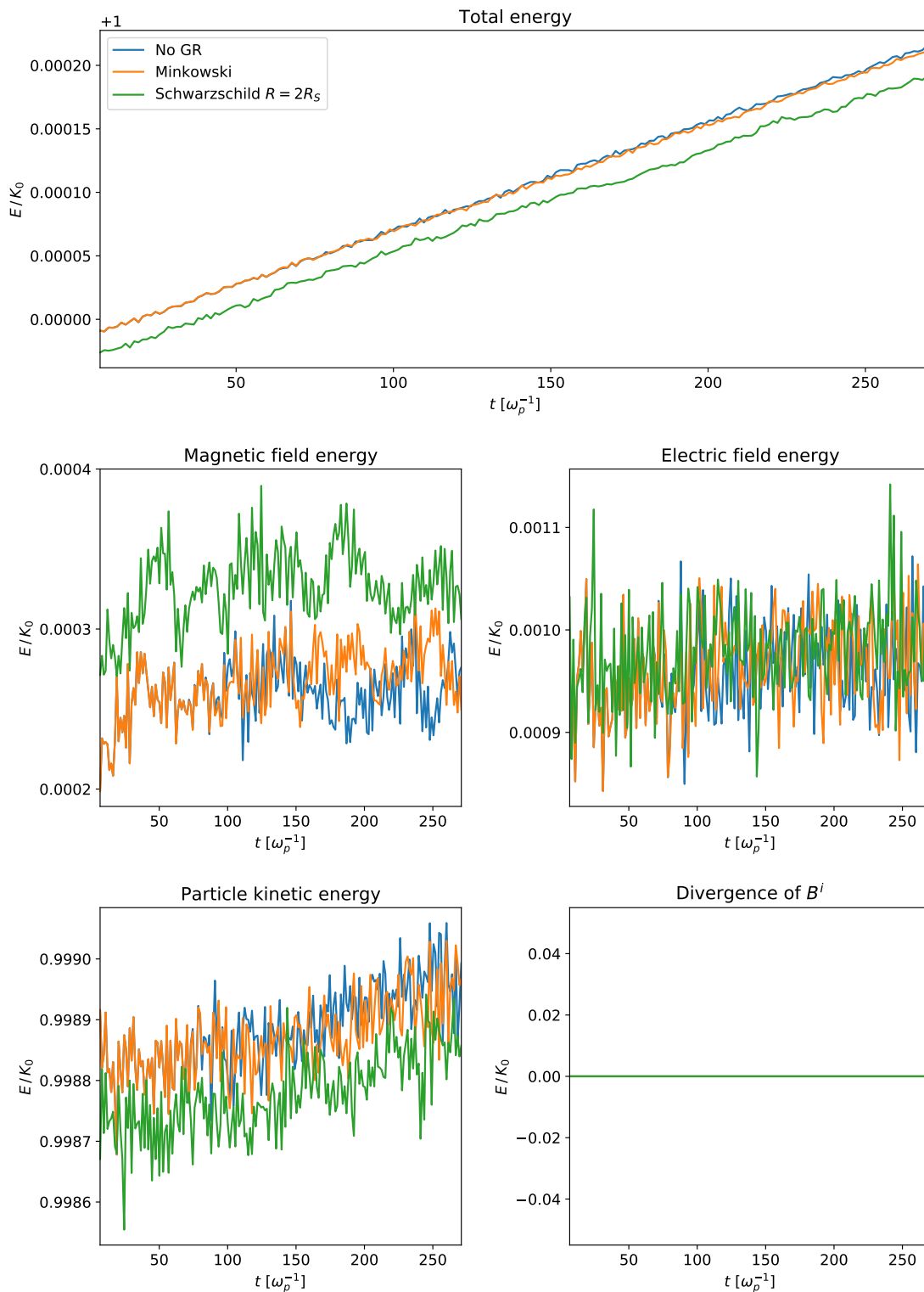


Figure 11: Energy components normalised to the initial kinetic energy of particles. The first 500 timesteps are cut off because of a jump in energy caused by the production of fields at the start of a simulation.

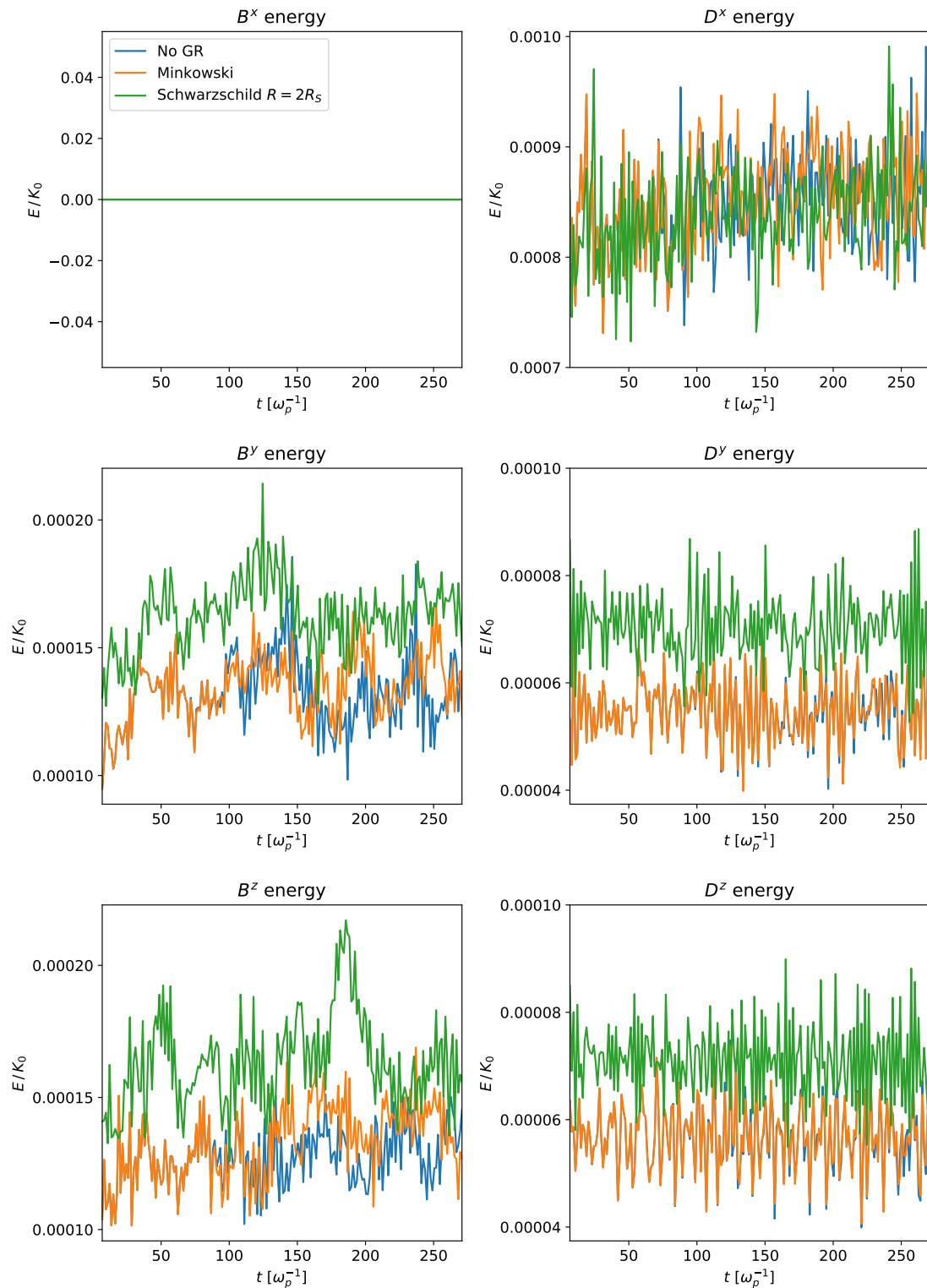


Figure 12: The same like in Figure (11), but for individual components of the electromagnetic field.

## 7.2 1D Plasma dispersion relations

To explore the properties of the simulated plasma further, a Fourier analysis was performed to investigate the plasma dispersion relations. The electric fields from the simulations described in the previous section were Fourier transformed with the help of the Python package *SciPy*. The Fourier transform decomposes the field into a series of periodic functions, where periodicity in the time dimension is described by the frequencies  $\omega$  and periodicity in the spatial dimensions by the wavenumber  $k$ . This allows us to identify the frequencies and wavenumbers that are most represented in the plasma waves. The dimensions of the original field and the dimensions of the Fourier transformed field are reciprocally bound. The bigger the simulation, either longer in time or space, the better the resolution in the frequencies or wavenumbers, respectively. The more temporally or spatially resolved the simulation is, the larger the range of frequencies or wavenumbers that can be identified.

Dispersion relations for Langmuir waves in strong gravitational fields have been analytically described by Elsässer and Popel (1997). Within the “3+1” formalism presented in this thesis, the dispersion relation for electrostatic Langmuir waves under the assumption that  $|k\lambda_D| \ll 1$  reads

$$\omega^2 = [\alpha^2(1 + 3k^2\lambda_D^2) - v_{th}^2\gamma_{||}] \omega_p^2 \Gamma, \quad (29)$$

$$\lambda_D = \frac{v_{th}}{\alpha\omega_p\sqrt{\Gamma}}, \quad (30)$$

where  $\alpha$  is the lapse function,  $v_{th}$  is the thermal velocity of the plasma,  $\gamma_{||}$  is the 3-metric component parallel to the wave propagation,  $\omega_p$  is plasma frequency and  $\Gamma = \sqrt{1 + v_{th}^2}$  is the Lorentz factor.

In 1D, the electric field component  $D^x$  contains only the Langmuir electrostatic waves, which are shown in Figure (13) for the Minkowski metric and the Schwarzschild metric. The frequency axis is normalised to the plasma frequency  $\omega_p$  calculated from equation (5). The horizontal axis is normalised by the Debye length  $\lambda_D$  calculated from equation (30). The Langmuir waves in the Minkowski metric remain unchanged and can be described by the classical dispersion relation (6). In the Schwarzschild metric the Langmuir waves are modified; the cut-off frequency is decreased, and the slope of the branches is shallower. The dispersion relation is well described by the general relativistic equation (29).

Electromagnetic waves appear in electric fields  $D^y, D^z$ . Figure (14) shows their Fourier transformation, revealing the dispersion relation of the electromagnetic waves in the plasma. The vertical axis describes the frequency normalised to the plasma frequency. The horizontal axis is just the wave number; no normalisation is required. The dispersion relation of the electromagnetic waves in the Minkowski

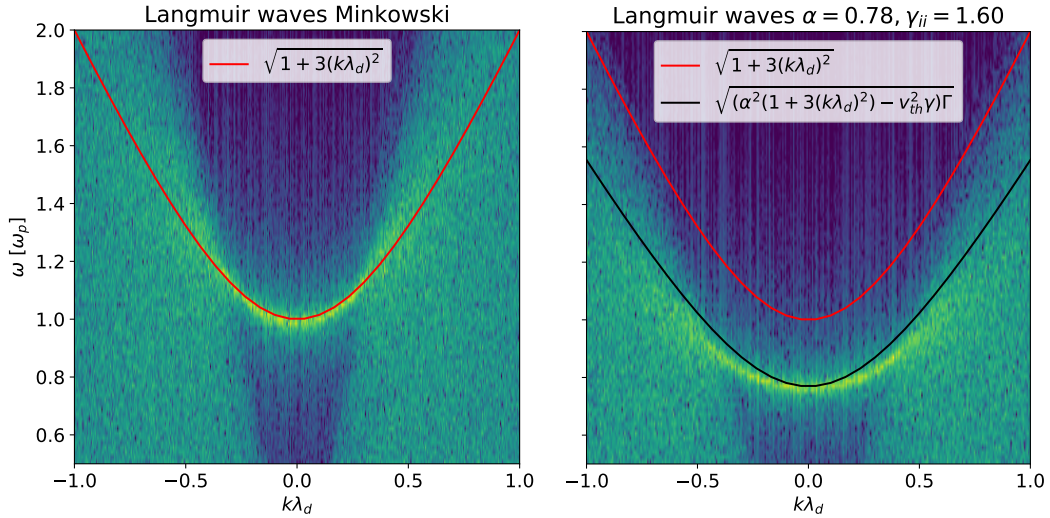


Figure 13: Fourier transformation of the electric field  $D^x$  in two simulations, left: Minkowski metric, right: constant metric with values of the Schwarzschild metric at  $R = 2R_S$ . The vertical axis is the frequency normalised to the plasma frequency  $\omega_p$ , the horizontal axis is the wavenumber normalised by the Debye length  $\lambda_D$ .

simulation agrees with the classical description in equation (9). In the Schwarzschild simulation, the dispersion relation is modified, and the classical description no longer holds. The dispersion relations are best described by the function

$$\omega^2 = \alpha^2 \omega_p^2 + \left( \frac{k}{\gamma_{||}} \right)^2. \quad (31)$$

We can see that the dispersion relations for both the electrostatic Langmuir waves and electromagnetic waves in a plasma depend on the parameters of the spacetime in which it is located. The change in dispersion relations also influences the phase and group velocity of the waves, influencing their propagation.

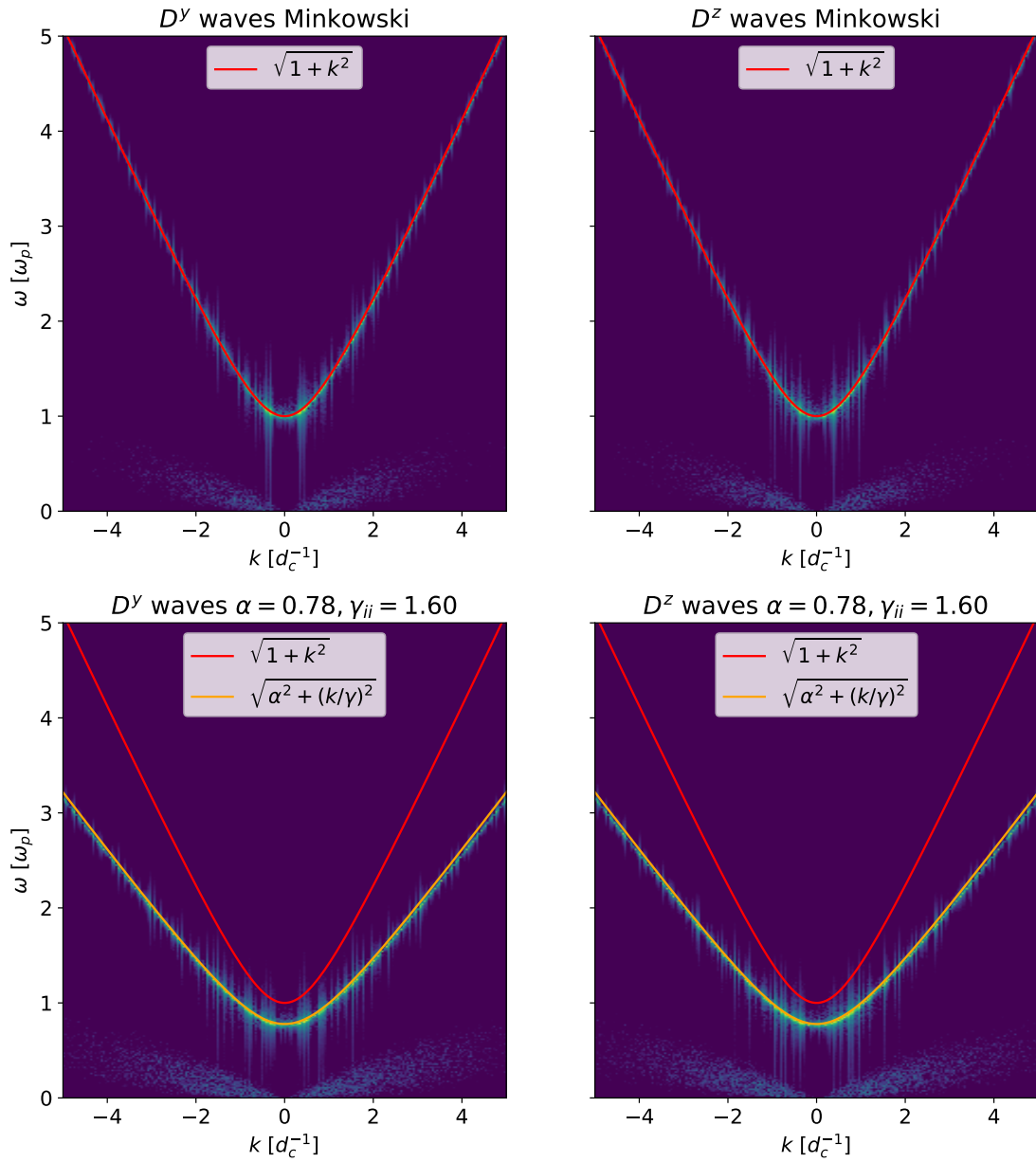


Figure 14: Fourier transformation of the electric fields  $D^y, D^z$  in different simulations, top: Minkowski metric, bottom: constant metric with values of the Schwarzschild metric at  $R = 2R_S$ . The vertical axis is the frequency normalised to the plasma frequency  $\omega_p$ , the horizontal axis is the wavenumber.

### 7.3 2D Thermal plasma

A pair of 2D simulations was run with a setup similar to that of the 1D simulations, one with the Minkowski metric, the second with the constant metric with values of the Schwarzschild metric at  $R = 2R_S$ . It was filled with plasma consisting of electrons and positrons with a Maxwellian velocity distribution with thermal velocity  $v_{th} = 0.1c$  and a density of 40 ppc. No external magnetic field was present. The simulations were run for 20000 timesteps with a temporal resolution normalised to the plasma frequency  $\Delta t\omega_p = 0.015$ , which gives approximately  $20000\Delta t\omega_p = 300$  plasma oscillations. A  $500 \times 500$  grid was used in the x- and y- direction with a spatial resolution  $\Delta x/d_c = 0.050$ , where  $d_c = c/\omega_p$  represents the skin depth, the distance light travels in one plasma oscillation. Then  $(\Delta x/d_c)^{-1} = 20$  is the number of cells light travels through during one plasma oscillation. The light travels  $300/(500/20) = 12$  times through the grid during the simulation time. The Courant number  $C = c\Delta t/\Delta x = 0.3$  satisfies the CFL condition, ensuring the numerical stability of the field solver. The boundary conditions were set to be periodic.

In 2D, the electrostatic Langmuir waves propagate in both the x- and y-direction and appear in the corresponding electric fields  $D^x, D^y$ . Furthermore, electromagnetic waves are generated and propagate in all components of the electric and magnetic field. The results of the simulations are shown in Figures (15) and (16). The electric fields  $D^x, D^y$  are dominated by the electric fields produced by plasma oscillations, and their granularity looks similar, while  $D^z$  consists purely of electromagnetic waves, and thus looks different with lower range of field strength. On the other hand, the magnetic fields in Figure (16) are purely electromagnetic waves. A preferred direction in the shape of the local perturbations is clearly visible in the x- and y-components of both the electric and magnetic fields. The  $D^x$  is prolonged in the y-direction, while  $B^x$  is prolonged in the x-direction. This anisotropy is probably tied to the difference in direction of propagation between the Langmuir waves and the electromagnetic waves.

The energy of the components of the simulation was investigated similarly to the 1D simulations. Figure (17) shows the total energy, the energy of the electric and magnetic field, the energy of particles and the divergence of  $B^i$ . All energies are normalised to the initial kinetic energy of particles. Due to the jump in energy at the start, the first 500 timesteps have been cut off in the figures. The total energy has a negligible linear growth over the time of the simulation in both cases. An increase in the magnetic field energy and a decrease in the energy of particles is seen in the Schwarzschild metric. The divergence is conserved throughout the simulation. Figure (18) shows the energy of the components of the electric and magnetic field. The energy of the components  $D^x$  and  $D^y$  do not change with the metric parameters, while the components connected to the electromagnetic waves have an increased energy in the Schwarzschild simulation. The modified metric

parameters in the Schwarzschild simulation amplify the jump in energy at the beginning of the simulation. This is also visible in the range of field strength in Figures (15) and (16), where the fields dominated by electromagnetic waves have a higher amplitude.

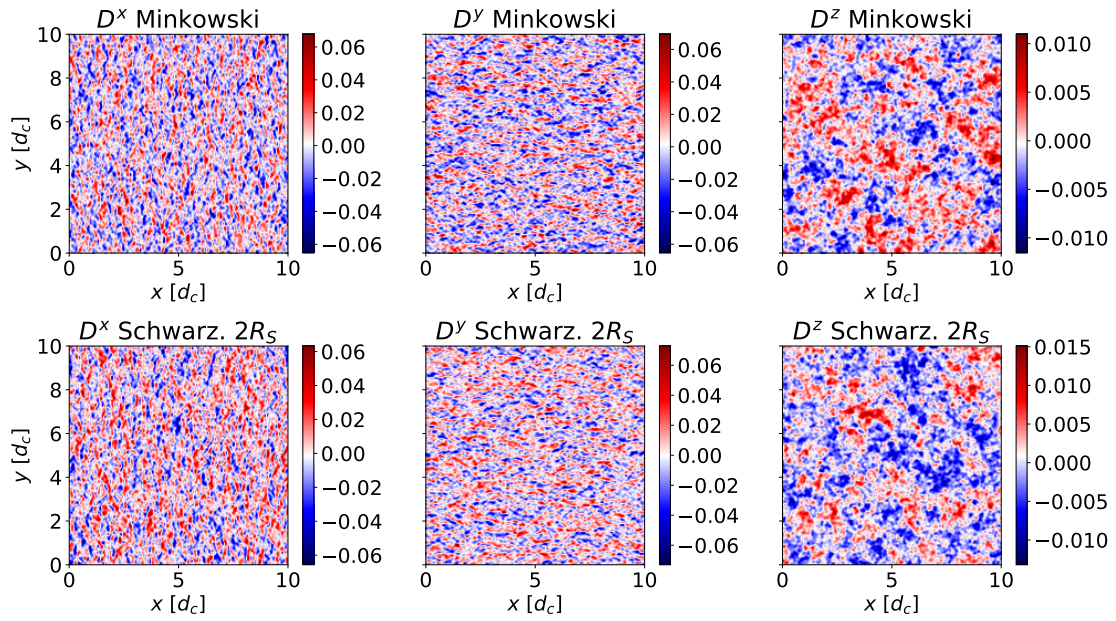


Figure 15: The electric field  $D^i$  at the end of the 2D simulation.

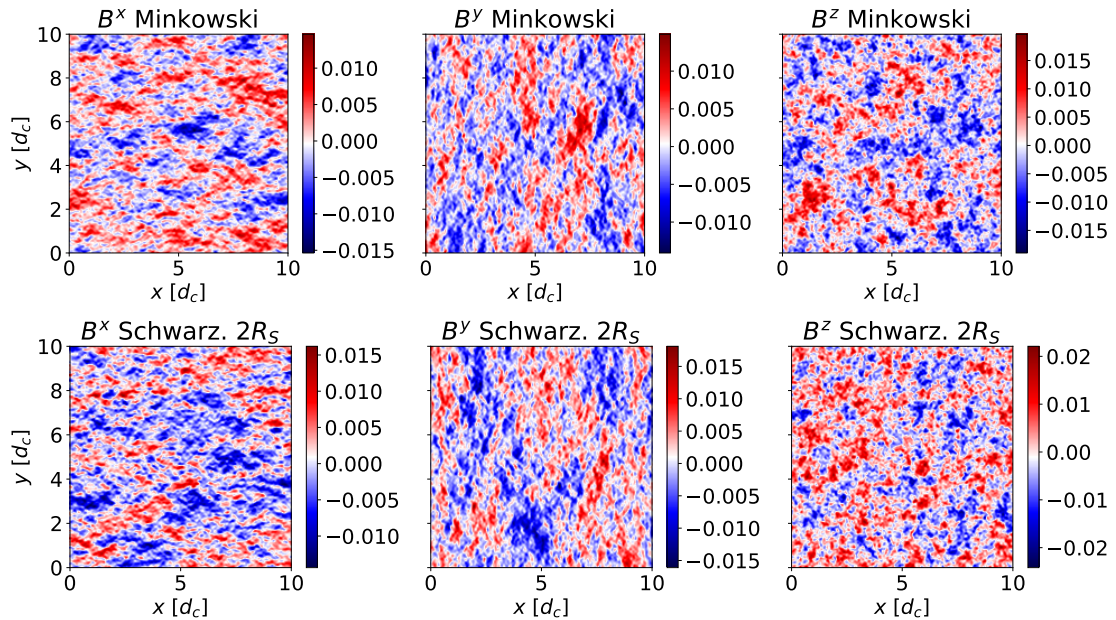


Figure 16: The magnetic field  $B^i$  at the end of the 2D simulation.

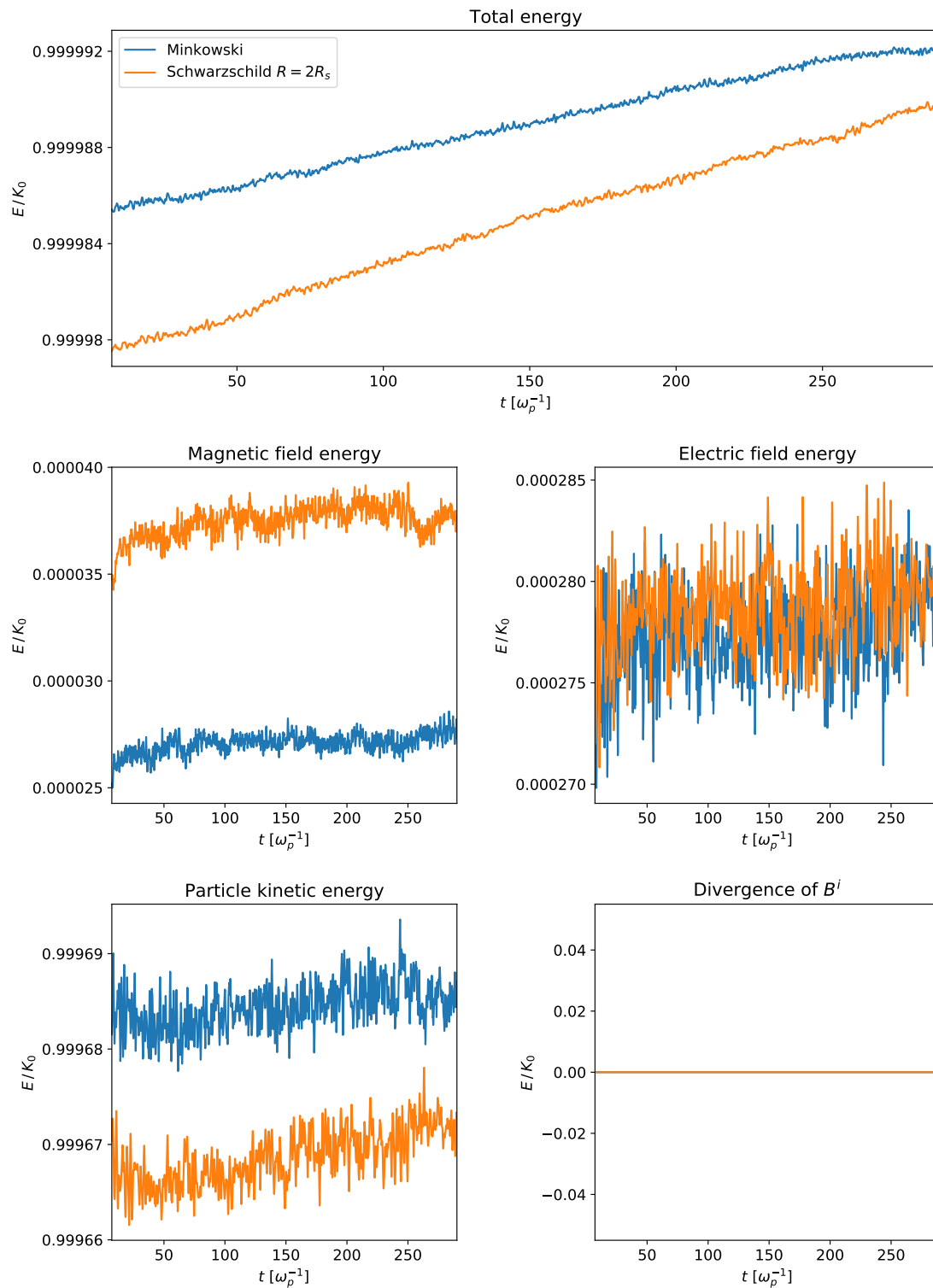


Figure 17: Energy components normalised to the initial kinetic energy of particles. The first 500 timesteps are cut off because of a jump in energy caused by the production of fields at the start of a simulation.

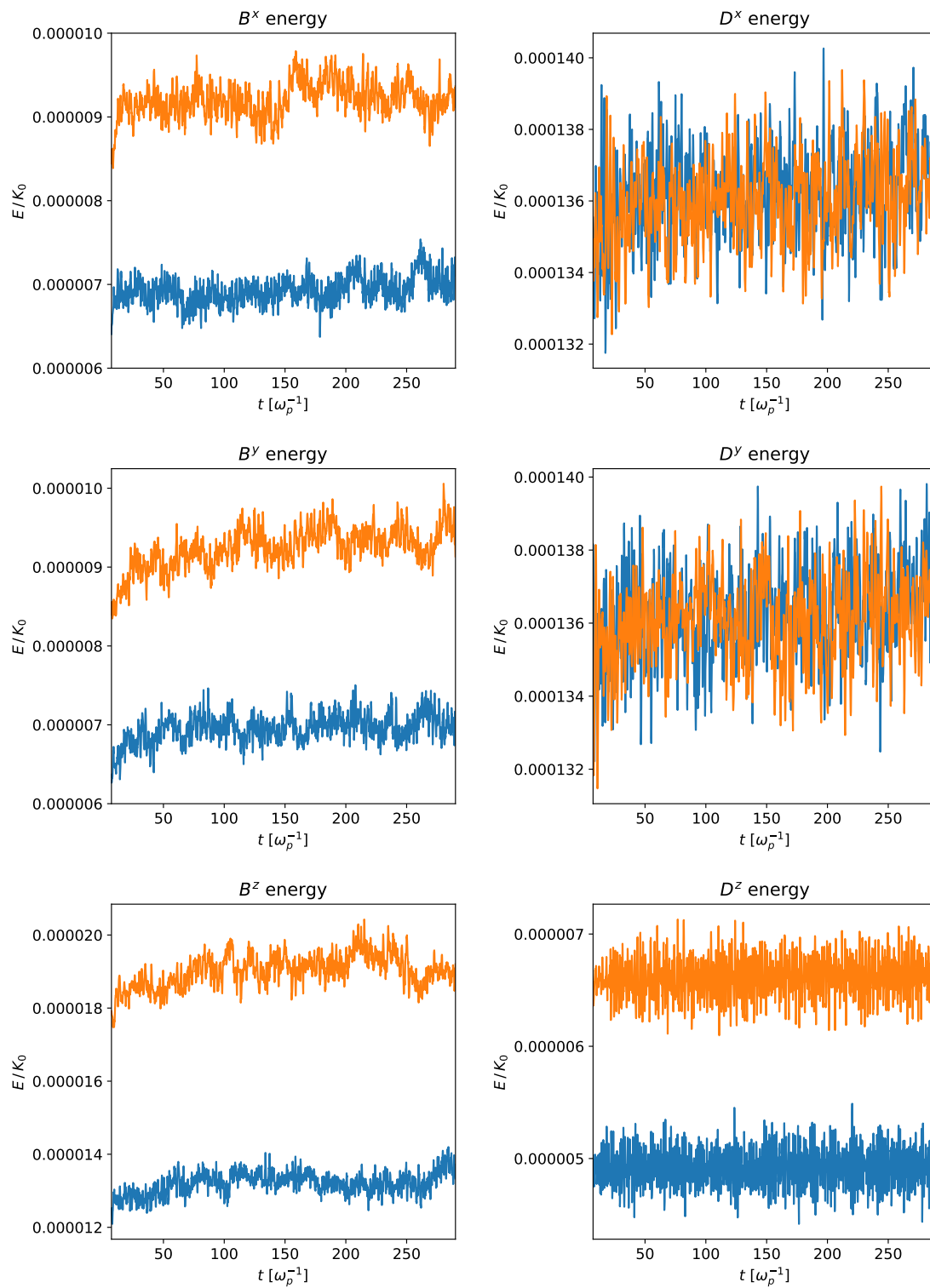


Figure 18: The same as in Figure (17), but for individual components of the electromagnetic field.

## 7.4 2D Plasma dispersion relations

A Fourier analysis of the electric fields of the 2D simulations was performed. Because there are one temporal and two spatial dimensions, the resulting Fourier image also has three dimensions, one represented as the frequency of the waves and two describing the wavevectors. The dispersion relations from equations (6) and (9) create a cylindrically symmetric surface. To plot the dispersion relations on a 2D plot, it has to be sliced along one spatial dimension. Depending on the dimension and position of the slice, the resulting image changes and describes waves propagating in different directions. For example, creating a slice in the  $k_x$ -direction at  $k_y = 0$  reveals waves propagating in the x-direction. Likewise, slicing in the  $k_y$ -direction at  $k_x = 0$  reveals waves propagating in the y-direction.

In our case, the Fourier transformation of the electric field  $D^x$  sliced at  $k_y = 0$  uncovers the dispersion relation of the electrostatic Langmuir waves seen in Figure 19, but a slice in the other direction at  $k_x = 0$  results in the dispersion relation of the electromagnetic waves, as seen in Figures (20) and (21). This is because, in 2D space, the Langmuir waves in  $D^x$  propagate only in the x-direction, whereas the electromagnetic waves in  $D^x$  propagate only in the y-direction.

Figure (19) shows the dispersion relations of electrostatic Langmuir waves appearing in the electric field  $D^x$ ,  $D^y$  and in the two aforementioned metrics. The top row depicts the Minkowski simulation, which behaves as expected. The cut-off frequency is located at the plasma frequency, and the branches are well described by the classical analytical equation (6). The bottom row shows the simulation with the constant Schwarzschild metric. The cut-off frequency is lowered mainly by the parameter  $\alpha$ , the term  $v_{th}^2 \gamma_{||}$  is only a tiny correction. The branches follow the dispersion relation from equation (29).

The electromagnetic waves are displayed in Figures (20) and (21). In electric fields  $D^x$  and  $D^y$  they propagate only in the perpendicular directions y and x, respectively. In  $D^z$  the waves propagate in both directions. The Minkowski simulation agrees with the classical description given by equation (9). The change in metric parameters in the constant Schwarzschild simulation changes the dispersion relations in accordance with equation (31). The cut-off frequency is decreased by the parameter  $\alpha$ , and the branches are shallower.

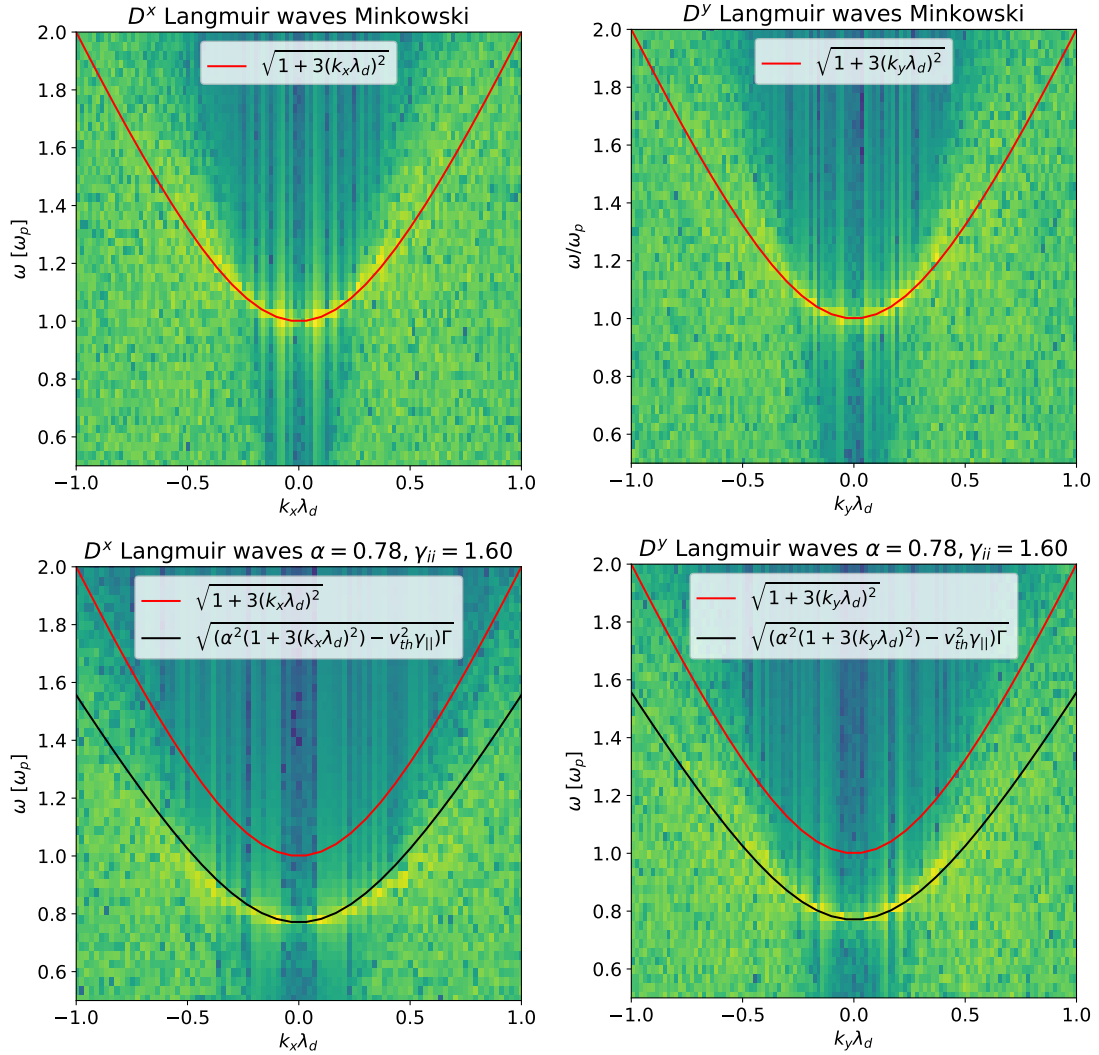


Figure 19: Dispersion relations of the electrostatic Langmuir waves in the electric field of the 2D simulations. Top: Minkowski metric, Bottom: constant metric with values of Schwarzschild metric at  $R = 2R_S$ . The axes of the figure are normalised by the plasma frequency  $\omega_p$  from equation (5) and the Debye length  $\lambda_D$  from equation (30).

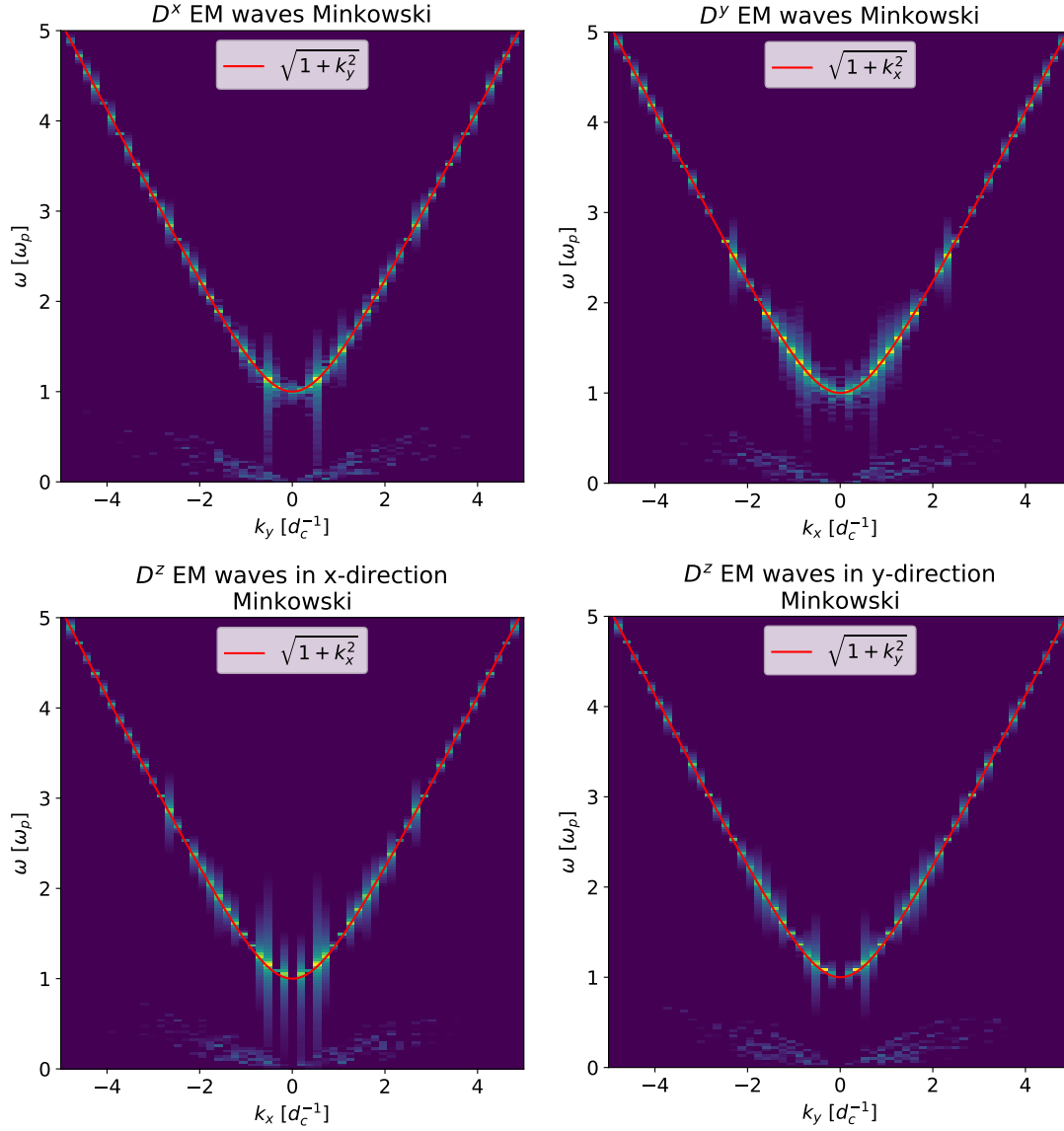


Figure 20: The Fourier transformed electric field of the 2D simulation with the Minkowski metric showing the dispersion relations of electromagnetic waves. The frequency axis is normalised to the plasma frequency  $\omega_p$  from equation (5).

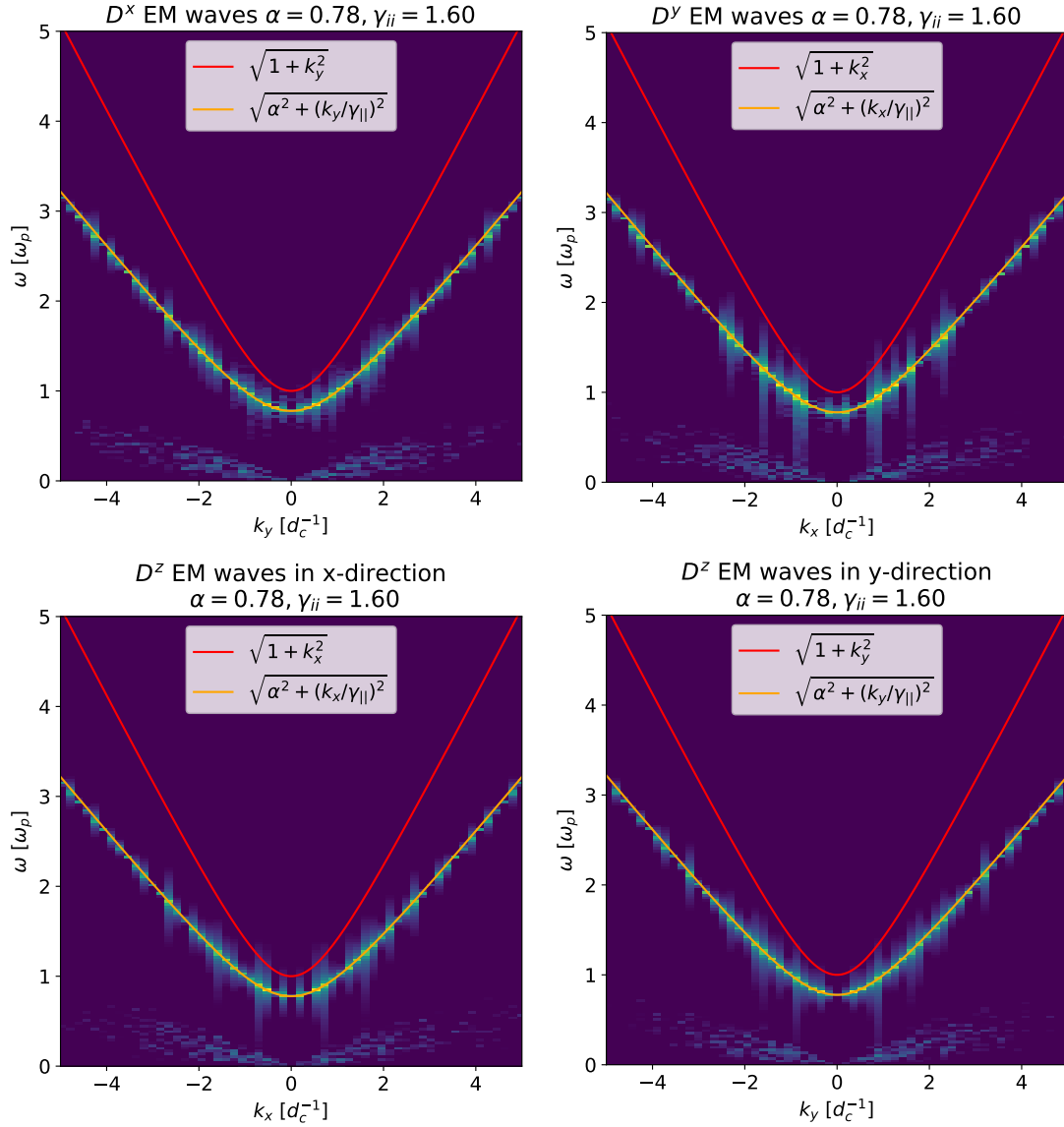


Figure 21: The Fourier transformed electric field of the 2D simulation with the constant metric with values of the Schwarzschild metric at  $R = 2R_S$  showing the dispersion relations of electromagnetic waves. The frequency axis is normalised to the plasma frequency  $\omega_p$  from equation (5).

## Conclusions

This thesis has introduced the basics of plasma physics and their modelling using particle-in-cell simulations. Following previous articles, the inclusion of spacetime parameters in the fundamental equations of the PIC method was presented with the aim of studying plasma in curved spacetime in compact object magnetospheres.

In Section 6, my 1D and 2D implementation of the modifications in the PIC code ACRONYM was presented. I modified the field solver to allow use in non-rotating curved spacetime, where the shift vector  $\beta^i = 0$ . I developed and implemented an interpolation scheme for the computation of the auxiliary fields  $E_i, H_i$  in non-diagonal 3-metrics that weights the fields based on the metric. I performed vacuum simulations of the propagation of an electromagnetic wave, which confirmed numerical stability of the modification. I investigated the propagation speed of the wave, which showed a direct relation with the metric parameters. Wave propagation was simulated in a curved Schwarzschild spacetime which confirmed numerical stability and physical accuracy of the field solver in a curved spacetime. Propagation was also tested in 2D space which confirmed the results of the 1D simulations and also showed anisotropic propagation in anisotropic spacetime.

I presented a modification to the Boris push along with an interpolation scheme of the field quantities to the particle positions, both designed for use in curved spacetime. I developed and implemented a novel approach to charge-conserving current deposition based on the Esirkepov scheme for use in non-rotating curved spacetime.

I ran a set of 1D and 2D simulations with thermal plasma and no external magnetic field for the Minkowski metric and a constant metric with the values of the Schwarzschild metric at  $R = 2R_S$ . The results confirmed the numerical stability of the modification and revealed changes in the electromagnetic field of the plasma depending on the chosen metric, specifically, an increase of field strength in components of the electromagnetic field dominated by electromagnetic waves in the constant Schwarzschild metric. The energy of the simulations also displayed changes depending on the curved spacetime. A slight increase in the growth of the total energy was found for the Schwarzschild metric in comparison to the Minkowski metric. The amplification of the fields dominated by electromagnetic waves in the Schwarzschild metric was also visible in the energy of those field components.

I performed a Fourier analysis on the 1D and 2D thermal plasma simulations. The dispersion relations of both electrostatic Langmuir waves and electromagnetic waves in the Minkowski metric were found to agree with the classical description in equations (6) and (9). In the Schwarzschild metric, the electrostatic Langmuir

waves behaved according to the general relativistic dispersion relations calculated by Elsässer and Popel (1997) in equation (29). The dispersion relations of the electromagnetic waves in the Schwarzschild metric changed based on the metric parameters and are described by equation (31).

At this stage, the implementation allows for the simulation of plasma in a non-rotating uncurved spacetime with a non-diagonal 3-metric. The periodic boundary conditions remain a problem that needs to be solved in order to eliminate the need to pad the metric parameter arrays at the boundaries to equal the Minkowski metric. A modification of the particle pusher for the calculation of the metric-induced terms in the acceleration equation is required to obtain the ability to simulate plasma in curved spacetime. Significant work is needed to include the shift vector  $\beta^i$  in the calculations to allow simulation of rotating systems. In particular, it is the implementation of the predictor-corrector scheme in the time evolution of the fields, the interpolation of the field components to the correct position in the Yee lattice for the calculation of the auxiliary fields in equations (21) and (22), and the modification of the particle pusher. A nice addition would be the expansion of the modification to 3D.

# References

- Blandford, Roger and Noémie Globus (Aug. 2022). “Jets, Disks and Winds from Spinning Black Holes: Nature or Nurture?” In: *Galaxies* 10.4, 89, p. 89. DOI: 10.3390/galaxies10040089. arXiv: 2207.05839 [astro-ph.HE].
- Boris, Jay P. and Ramy A. Shanny (1971). “Proceedings, Fourth Conference on the Numerical Simulation of Plasmas : November 2, 3, 1970, Naval Research Laboratory, Washington, D.C.” In: URL: <https://api.semanticscholar.org/CorpusID:107199562>.
- Carroll, Bradley W. and Dale A. Ostlie (2017). *An introduction to modern astrophysics, Second Edition*.
- Carroll, Sean M. (Dec. 1997). “Lecture Notes on General Relativity”. In: *arXiv e-prints*, gr-qc/9712019, gr-qc/9712019. DOI: 10.48550/arXiv.gr-qc/9712019. arXiv: gr-qc/9712019 [gr-qc].
- Cerutti, Benoît (2021). “Particle acceleration in relativistic magnetospheres”. PhD thesis. Université Grenoble Alpes. URL: [https://ipag.osug.fr/~ceruttbe/documents/bcerutti\\_hdr.pdf](https://ipag.osug.fr/~ceruttbe/documents/bcerutti_hdr.pdf).
- Chen Francis F., 1929- (1984). *Úvod do fyziky plazmatu*. Ed. by 1941- Rohlena Karel. Vyd. 1. Praha: Academia. URL: <http://www.ndk.cz/>.
- Crinquand, Benjamin (July 2021). “Particle acceleration in Kerr black hole magnetospheres”. Theses. Université Grenoble Alpes [2020-....] URL: <https://theses.hal.science/tel-03406333>.
- Elsässer, Klaus and Sergey I. Popel (1997). “Plasma equations in general relativity”. In: *Physics of Plasmas* 4, pp. 2348–2356. URL: <https://api.semanticscholar.org/CorpusID:123470576>.
- Esirkepov, T.Zh. (2001). “Exact charge conservation scheme for Particle-in-Cell simulation with an arbitrary form-factor”. In: *Computer Physics Communications* 135.2, pp. 144–153. ISSN: 0010-4655. DOI: [https://doi.org/10.1016/S0010-4655\(00\)00228-9](https://doi.org/10.1016/S0010-4655(00)00228-9). URL: <https://www.sciencedirect.com/science/article/pii/S0010465500002289>.
- Hewish, A. et al. (Feb. 1968). “Observation of a Rapidly Pulsating Radio Source”. In: *Nature* 217.5130, pp. 709–713. DOI: 10.1038/217709a0.
- Komissarov, S. S. (May 2004). “Electrodynamics of black hole magnetospheres”. In: *MNRAS* 350.2, pp. 427–448. DOI: 10.1111/j.1365-2966.2004.07598.x.
- Longair, Malcolm S. (2011). *High Energy Astrophysics*.
- Philippov, A. and M. Kramer (Aug. 2022). “Pulsar Magnetospheres and Their Radiation”. In: *ARA&A* 60, pp. 495–558. DOI: 10.1146/annurev-astro-052920-112338.

Schutz, Bernard F. (2022). *A first course in general relativity*. DOI: 10.1017/9781108610865.

Yee, Kane (May 1966). “Numerical solution of initial boundary value problems involving maxwell’s equations in isotropic media”. In: *IEEE Transactions on Antennas and Propagation* 14.3, pp. 302–307. DOI: 10.1109/TAP.1966.1138693.